

Spectroscopically resolved resonant interatomic Coulombic decay in photoexcited large He nanodroplets

L. Ben Ltaief^{1,*}, K. Sishodia², R. Richter³, B. Bastian¹, J. D. Asmussen¹, S. Mandal⁴, N. Pal³, C. Medina⁵, S. R. Krishnan⁶, K. von Haefen^{7,†} and M. Mudrich^{1,‡}

¹*Department of Physics and Astronomy, Aarhus University, 8000 Aarhus C, Denmark*

²*Quantum Center of Excellence for Diamond and Emergent Materials and Department of Physics, Indian Institute of Technology Madras, Chennai 600036, India*

³*Elettra-Sincrotrone Trieste, 34149 Basovizza, Trieste, Italy*

⁴*Indian Institute of Science Education and Research, Pune 411008, India*

⁵*Institute of Physics, University of Freiburg, 79104 Freiburg, Germany*

⁶*Department of Physics, Indian Institute of Technology, Madras, Chennai 600 036, India*

⁷*DESY, Notkestraße 85, 22607 Hamburg, Germany*



(Received 24 August 2023; accepted 28 November 2023; published 8 January 2024)

Interatomic Coulombic decay (ICD) processes play a crucial role in weakly bound complexes exposed to intense or high-energy radiation. Using large helium nanodroplets, we demonstrate that ICD is efficient even when the droplets are irradiated by weak synchrotron radiation at relatively low photon energies. Below the ionization threshold, resonant excitation of multiple centers efficiently induces resonant ICD as previously observed for intense pulses [A. C. LaForge *et al.*, *Phys. Rev. X* **11**, 021011 (2021)]. More surprisingly, we observe ICD even above the ionization threshold due to recombination of photoelectrons and ions into excited states which subsequently decay by ICD. This demonstrates the importance of secondary processes, in particular electron scattering and recombination, in inducing ICD in extended condensed phase systems. High-resolution ICD electron spectra in combination with coincidence imaging of electrons and ions reveal the relaxation dynamics of highly excited and ionized weakly bound nanosystems.

DOI: [10.1103/PhysRevResearch.6.013019](https://doi.org/10.1103/PhysRevResearch.6.013019)

I. INTRODUCTION

When matter is exposed to ionizing radiation, both primary ionization and secondary processes may occur. In biological tissue, radiation damage is mostly induced by the latter, e.g., by multiple scattering of the primary photoelectron in the medium followed by dissociative attachment of low-energy electrons to vital biomolecules [1]. Another process creating slow, genotoxic low-energy electrons is interatomic Coulombic decay (ICD), where the energy deposited in one atom or molecule is transferred to another which in turn is ionized [2].

ICD has been discovered and characterized in detail for small van der Waals (vdW) molecules and clusters [2,3]. More recently, the focus has shifted to more relevant condensed-phase systems such as liquid water [4,5]. There, the light-matter interactions are more complex and the processes causing radiation damage are harder to decipher; in

particular electron scattering tends to obscure the signatures of ICD in electron spectra [6].

ICD induced by resonant excitation of an atom in an environment has been termed resonant ICD [4,7,8]. While originally an inner valence shell electron was excited to trigger resonant ICD [7], it also occurs in multiply outer-valence-shell excited clusters [9]. With the advent of free electron lasers (FELs) that generate intense, tunable extreme ultraviolet (EUV) radiation [10,11], new types of resonant ICD have been observed in rare-gas clusters and nanodroplets induced by absorption of multiple photons per cluster [9,12–16].

In this work, we report on observation of resonant ICD in resonantly excited large He nanodroplets after irradiation with weak synchrotron radiation. By employing high-resolution electron spectroscopy and electron and ion imaging spectroscopy, we show that even weak quasicontinuous synchrotron radiation can efficiently induce multiple excitations in large He nanodroplets leading to resonant ICD, as previously observed for intense FEL pulses [16]. Moreover, we find that elastic electron scattering can facilitate ICD by inducing electron-ion recombination into highly excited states which subsequently decay by resonant ICD. The goal is to unravel the mechanisms and efficiencies of ICD in large He nanodroplets in different regimes of excitation and near-threshold ionization.

He nanodroplets are a special type of condensed-phase system owing to their quantum fluid nature [17]. Atoms and

*ltaief@phys.au.dk

†Present address: Kanano GmbH, Sedanstraße 14, 89077 Ulm, Germany.

‡mudrich@phys.au.dk

Published by the American Physical Society under the terms of the [Creative Commons Attribution 4.0 International](https://creativecommons.org/licenses/by/4.0/) license. Further distribution of this work must maintain attribution to the author(s) and the published article's title, journal citation, and DOI.

molecules inside them are highly mobile, and electronically excited species tend to form void bubbles which are expelled to the droplet surface [18]. In contrast to other nanoclusters, the electron spectra of He nanodroplets are often well resolved [15,16,19–21]. However, electron scattering leading to low-energy electrons and electron-ion recombination occurs in other types of condensed-phase systems as well [22]. In particular, the decay of multiple excited states or excitons by ICD-type processes has been observed for solid rare-gas clusters [12,23], nanoplasmas [20,24–26], solid nanostructures [27], and thin films [28–30].

He nanodroplets have previously proven well suited as a model system for elucidating ICD and related processes. In those studies, either high-energy photons were used to excite into high-lying or ionized states of He [31–35], or intense pulses multiply excited or ionized the droplets [13–16,20,24–26,36]. Using EUV pulses from a tunable FEL, the transition from the regime of ICD of weakly excited He droplets to the regime of ultrafast collective autoionization (CAI) of multiply excited He droplets was tracked [13,15]. EUV-pump, UV-probe studies of multiply excited He droplets indicated that ICD predominantly occurs in pairs of nearest-neighbor He* excited atoms within $\gtrsim 0.4$ ps, facilitated by the merger of void bubbles forming around each He* [16].

An important aspect of the present study is that only weak radiation with photon energies below or just above the ionization threshold of He is used for inducing resonant ICD. The He droplets are multiply excited or ionized owing to their large size, $\gtrsim 20$ nm, and absorption cross section, $\gtrsim 10^5 \text{ \AA}^2$. In such bulklike systems, inelastic and multiple elastic scattering efficiently slows down photoelectrons such that they are recaptured by the photoions to populate both fluorescing and metastable states, denoted as He* [35,37,38]. Resonant ICD then proceeds in the droplets according to the reaction $\text{He}^* + \text{He}^* \rightarrow \text{He} + \text{He}^+ + e_{\text{ICD}}^-$ [9]. Our results match well with a physical picture of metastable excited He* which migrate to and meet at the surface of the He droplets.

Additionally, by measuring the energy of the emitted ICD electron e_{ICD}^- , we gain detailed insight into the relaxation of the photoexcited system. We find that different states of He* are populated prior to ICD in the different regimes of resonant excitation, autoionization, or direct photoionization of the droplets. This is in agreement with previous studies of the relaxation dynamics of singly excited He droplets, which have shown that electronically excited He droplets relax into the lowest excited singlet state $1s2s \ ^1S$ within $\lesssim 1$ ps [18,39–41]. When the droplets are excited above their adiabatic ionization energy $E_i^{\text{drop}} \approx 23$ eV, additionally triplet states are populated by electron-ion recombination which relax by fluorescence emission and droplet-induced electronic relaxation into the metastable $1s2s \ ^3S$ state [40,42]. Surprisingly, the ICD spectra reveal that in large He droplets, electronic relaxation into the $1s2s \ ^1S$ state occurs even well above E_i^{drop} and recombination into the $1s2s \ ^3S$ state occurs up to several eV above the vertical ionization threshold of He, $E_i = 24.6$ eV. Thus, in extended systems, multiple electron scattering and electron-ion recombination is another efficient route to creating multiple excitations which subsequently decay by ICD.

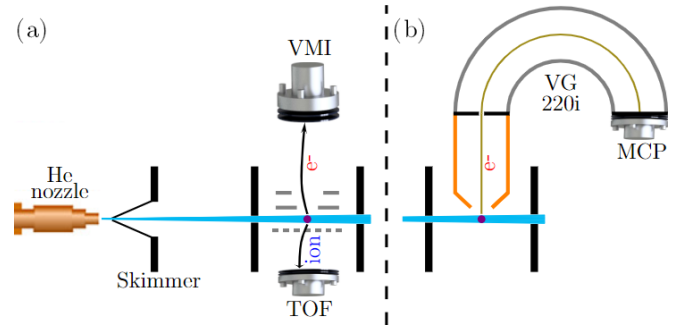


FIG. 1. Sketch of the experimental setups used in this work. (a) He nanodroplet beam source and coincidence velocity-map imaging (VMI) time-of-flight (TOF) spectrometer. (b) Hemispherical electron analyser (HEA) coupled to a microchannel plate (MCP) detector.

II. EXPERIMENTAL SETUP

To probe the ICD electrons emitted from He droplets at variable photon energy, a He nanodroplet apparatus combined with a photoelectron-photoion coincidence velocity-map imaging (PEPICO-VMI) detector [43] was used at the GasPhase beamline of the Elettra synchrotron facility in Trieste, Italy. The advantages of this technique are that (i) electron spectra inferred from VMI span the full energy range from zero to the maximum electron energy (typically 20–100 eV), (ii) electron angular distributions can be obtained, and (iii) electron spectra and angular distributions are detected for specific fragmentation channels by filtering the data according to the mass of the detected ion. Electron spectra were inferred from the VMI using the maximum entropy velocity legendre reconstruction (MEVELER) inversion method which is numerically efficient and robust with respect to noise [44]. In a second arrangement, a hemispherical electron analyser (HEA, model VG-220i) was mounted at the magic angle and combined with the He nanodroplet apparatus to measure high-resolution ICD electron spectra (see Fig. 1). Advantages of the HEA are (i) its high resolution of < 0.1 eV, (ii) the possibility to “zoom” into a small range of the electron spectrum while suppressing electrons whose energies lie outside this range, and (iii) the selective detection of electrons emitted in a small acceptance volume. In this way, spurious electrons emitted from the residual gas along the photon beam and from stray light hitting spectrometer surfaces are suppressed. The magic-angle geometry is chosen to ensure that the measured yields of electrons are independent of their angular distributions.

The He droplet apparatus has been described in detail elsewhere [45,46]. Briefly, a continuous beam of He nanodroplets of variable droplet radii ranging from $R = 5$ nm for droplets containing an average number of He atoms $\langle N \rangle \sim 10^4$ up to $R = 75$ nm ($\langle N \rangle \sim 10^8$) is generated by expanding He out of a cryogenic nozzle at a temperature ranging from 16 down to 8 K at 50 bar of He backing pressure. A mechanical chopper is used for discriminating the He droplet beam-correlated signals from the background.

In this study, the photon energy was tuned in the range $h\nu = 21.0\text{--}28.0$ eV, i.e., across the He absorption resonances

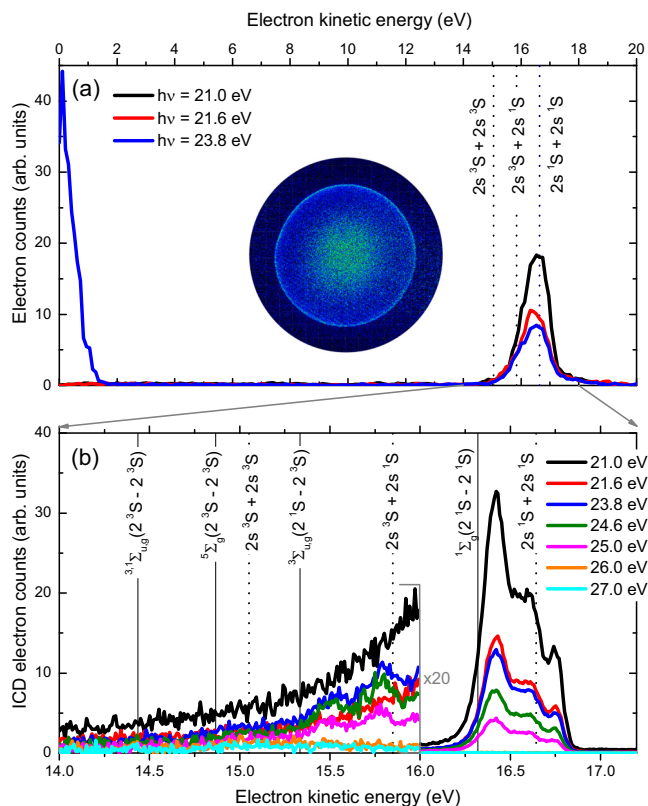


FIG. 2. Background-subtracted total electron spectra measured for pure large He nanodroplets ($R = 75$ nm) at different photon energies near the ionization energy of He using (a) the VMI spectrometer and (b) the HEA. The inset in (a) shows a raw total VMI recorded at $h\nu = 21.0$ eV. For better visibility, all of the spectra shown in (b) in the kinetic energy range 14.0–16.0 eV are scaled up by a factor of 20. All electron spectra are normalized to the flux of the incident EUV photon beam.

and across E_i . The use of a variable-angle spherical grating monochromator ensured narrow-band radiation with a time-averaged photon flux $\Phi \approx 5 \times 10^{11} \text{ s}^{-1}$.

III. RESULTS AND DISCUSSION

A. Total electron and EUV fluorescence spectra

The strongest resonant absorption bands of large He nanodroplets are those correlating to the $1s2s \ ^1S$ and $1s2p \ ^1P$ states of He atoms at photon energies $h\nu = 21.0$ and $h\nu = 21.6$ eV, respectively [45,47]. As these excitation energies stay below the adiabatic ionization energy E_i^{drop} , no direct electron emission is expected. Nevertheless, high yields of electrons are detected when the size of the He nanodroplets exceeds $R \approx 20$ nm [see Figs. 3(a) and 4(a)].

Electron VMI measured under these conditions displays a sharp-edged, perfectly isotropic ring structure [see the inset in Fig. 2(a)] recorded at $h\nu = 21.0$ eV. The total electron spectra shown in Fig. 2(a) are inferred from VMI recorded at $h\nu = 21.0$ eV (black line), $h\nu = 21.6$ eV (red line), and $h\nu = 23.8$ eV (blue line). All electron spectra exhibit a sharp peak around 16.6 eV. At $h\nu = 23.8$ eV, an additional narrow feature close to zero electron kinetic energy is present in

the spectrum which is due to autoionization of superexcited He droplets [19,48,49]. The peak present in all three spectra is centered at the electron energy expected for ICD of two He* in $1s2s \ ^1S$ states, $E_e = 2E_{1S} - E_i = 2 \times 20.6 \text{ eV} - 24.6 \text{ eV} = 16.6 \text{ eV}$, irrespective of $h\nu$. Here, E_{1S} is the excitation energy of the $1s2s \ ^1S$ state. This indicates that the He droplets mostly relax from the initially excited $1s2s$ -, $1s2p$ -, and $1s3p$ -correlated states of the droplet into the lowest excited $1s2s \ ^1S$ singlet state of the He* atom prior to ICD. Fast vibronic relaxation preceding ICD has been observed before [16,21]. This sets a lower bound to the ICD decay time to $\gtrsim 1$ ps, the relaxation time of electronically excited He droplets previously measured by time-resolved photoelectron spectroscopy [18,39–41].

This ICD process was previously observed using FEL pulses at much higher intensity, $\gtrsim 10^9 \text{ W cm}^{-2}$ [15,16], but not unambiguously using synchrotron radiation [19,21,46,49–53]. This is due to the low probability for multiple excitation of one nanodroplet by synchrotron radiation which has much lower intensity. However, in the following we show that large He droplets can indeed absorb multiple photons even from synchrotron radiation at intensities $\lesssim 0.1 \text{ W cm}^{-2}$. In the present experiment the He droplets were produced by supercritical expansion of liquid He; in this regime the droplets are much larger (radius $R > 10$ nm, $\langle N \rangle > 10^5$ He atoms per droplet) than those conventionally used for He-nanodroplet isolation spectroscopy, $\langle N \rangle \lesssim 10^4$ [54]. Accordingly, their absorption cross section is larger and the rate of resonant absorption of a droplet with, e.g., $\langle N \rangle = 10^6$ is $r_{\text{abs}} = \sigma_{2p} \langle N \rangle \Phi / w^2 \approx 10^4 \text{ s}^{-1}$. Here, the photon beam radius is $w \approx 300 \mu\text{m}$ and the absorption cross section at the $1s2p$ resonance of He droplets at $h\nu = 21.6$ eV is estimated to $\sigma_{2p} = 25 \text{ Mbarn}$ [13,46]. Accordingly, the probability that such a droplet resonantly absorbs one photon during its flight through the interaction region is $p_1 = \sigma_{2p} \langle N \rangle t_{\text{tr}} \Phi / w^2 \approx 1\%$ for a transit time of the droplets through the focus $t_{\text{tr}} \approx 1 \mu\text{s}$. As it takes two photons to excite a pair of He* atoms in one droplet which subsequently decay by ICD, the ICD rate is $r_{\text{ICD}} \approx r_{\text{abs}}/2$, assuming a unity probability that ICD occurs in a pair of He*s [9]. For an estimated number density of He droplets in the jet of $n_{\text{HeN}} \sim 10^6 \text{ cm}^{-3}$ and an active length of the focal volume of $d \approx 2$ mm, the total ICD rate is $R_{\text{ICD}} = r_{\text{ICD}} n_{\text{HeN}} w^2 d \approx 10^6 \text{ s}^{-1}$. This value roughly matches the rate of detected ICD electrons in the experiment considering the detection efficiency of the HEA is $\sim 10^{-3}$.

Note that $R_{\text{ICD}} \propto \Phi$ scales linearly with photon flux Φ although two or more photons have to be absorbed by one He droplet to induce ICD. Only for much higher intensity as in previous FEL experiments would the excited-state population and hence R_{ICD} be saturated [13,14]. This linear dependency of R_{ICD} on Φ is experimentally confirmed (see Fig. 10 in Appendix A). When varying the photon flux by gradually opening and closing the exit slit of the monochromator and measuring all ICD electrons produced at $h\nu = 21$ eV, we observe essentially a linear dependency over more than one order of magnitude variation of the photon flux, irrespective of the He nanodroplets size.

Using the HEA, the ICD features seen at the electron energy $E_e = 16.6$ eV in the VMI spectra are much better resolved. Figure 2(b) shows high-resolution total electron

spectra measured using the HEA at various photon energies below and above E_i . The spectra clearly show a substructure of the ICD peak. Additionally, a low-amplitude wing structure extends from $E_e = 16.2$ eV down to about 14 eV, indicating that $1s2s\ ^3S$ -excited He^* atoms and correlated states of the He_2^{**} dimer contribute to the ICD signal to a small extent. ICD electrons that lose kinetic energy by elastic scattering at He atoms in the droplets likely contribute to this wing structure, in particular at $h\nu = 21$ and 21.6 eV [38,50,51]. The main ICD peak at these photon energies exhibits one peak at $E_e = 16.4$ eV originating from ICD of pairs of He^* 's in the $^1\Sigma_g$ state correlating to two atoms each in the $1s2s\ ^1S$ state [16], and a shoulder that extends up to 16.8 eV featuring two smaller peaks. This feature closely resembles the one previously observed for subthermal binary collisions of He^* atoms in an atomic jet [55,56]. The oscillatory structure was interpreted as a quantum interference effect in the entrance channel of the pair of colliding metastable atoms. The lack of any distortion of the ICD electron spectra caused by the He droplet indicates that ICD takes place in pairs of He^* atoms that have emerged from the bulk of the droplets to the surface where they remain weakly bound [57].

Electron spectra recorded in the droplet autoionization regime at $23.8 \leq h\nu \leq 24.6$ eV exhibit two small maxima at 15.5 and 15.8 eV in addition to the main ICD features. They can be ascribed to ICD out of $^3\Sigma_{g,u}$ states correlating to a mixed pair of metastable $\text{He}^*(^1S, ^3S)$. The structure of these two peaks resembles very well the structure of electron spectra previously observed in the binary collision experiments [55,56]. Interestingly, these two small peaks that involve the $1s2s\ ^3S$ states only appear in the electron spectra at $h\nu \geq E_i^{\text{drop}} = 23$ eV. The main ICD features around $E_e = 16.5$ eV are still visible up to $h\nu = 25.0$ eV and disappear for $h\nu \geq 26.0$ eV whereas the small peaks at $E_e < 16$ eV are still faintly visible. This implies that autoionization and photoionization are followed by electron-ion recombination, leading to the formation of He^* in the metastable $1s2s\ ^3S$ state which in turn undergoes ICD by interaction with another $1s2s\ ^3S$ or $1s2s\ ^1S$ He^* atom [40,42]. Note that formation of metastable triplet states by electron-ion recombination was previously reported in He_2^+ ion-electron collision experiments and theoretical works [58,59]. It was found that electron capture by He_2^+ and the ensuing dissociative recombination (DR) preferentially leads to the population of He^* in triplet states. The structure of the high-resolution ICD electron spectra between $E_e = 16.0$ and 17.0 eV in Fig. 2(b) will be discussed in more detail in Sec. III C.

To get an overview of the ICD efficiency across the entire photoexcitation spectrum of He droplets, the photon energy was tuned from $h\nu = 20$ to 26.5 eV while measuring the yield of all ICD electrons with the HEA. Figure 3(a) shows the HEA signal integrated in the electron energy range $E_e = 16$ –17 eV for He droplets of various sizes in the range $R = 6$ –75 nm. The ICD yield spectra exhibit four main features: A sharp peak at $h\nu = 21.0$ eV associated with the $1s2s\ ^1S$ droplet resonance and two broad features peaked at $h\nu = 21.4$ and $h\nu = 23.8$ eV associated with the $1s2p\ ^1P$ and $1s3p/1s4p$ droplet states, respectively [47,60]. A fourth maximum appears at $h\nu = E_i = 24.6$ eV, where a high density of Rydberg states is expected. These features

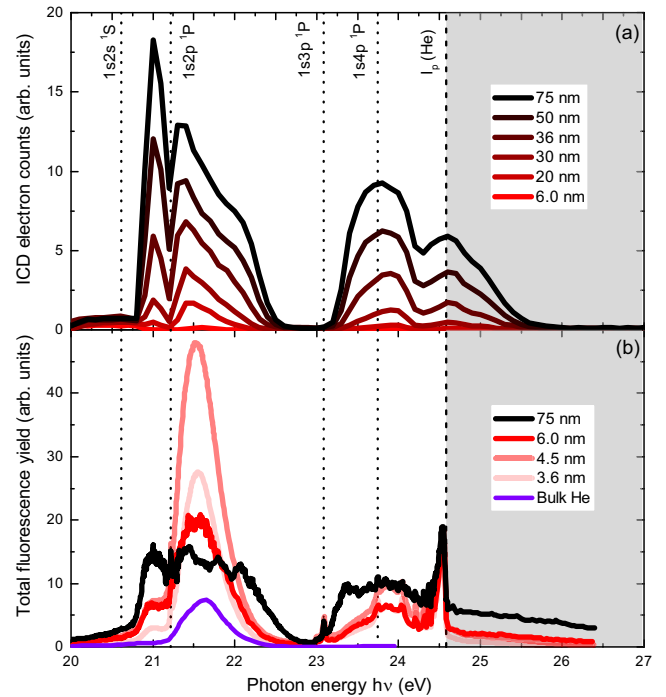


FIG. 3. Total yield spectra of (a) ICD electrons and (b) EUV fluorescence measured for He nanodroplets of various sizes. The EUV fluorescence data shown in (b) are reproduced from Ref. [60]. All curves are background corrected and normalized to the photon flux. The purple line is the absorption spectrum of bulk liquid He taken from Ref. [61].

are invisible for small droplets ($R < 20$ nm) [see red line in Fig. 3(a)]. They are clearly visible at $R = 20$ nm and become more and more pronounced when the droplet radius is further increased to $R = 75$ nm and at the same time the total number of He atoms in the focal volume rises [black line in Fig. 3(a)].

For comparison, Fig. 3(b) shows previously measured EUV fluorescence yield spectra of He nanodroplets (red lines) [60]. The dark line, showing the EUV fluorescence spectra for the largest He droplets ($R = 75$ nm), features a similarly distorted peak structure as the ICD spectra; the $1s2s\ ^1S$ -correlated peak at $h\nu = 21.0$ eV is enhanced, the $1s2p\ ^1P$ -correlated peak at $h\nu = 21.6$ eV is flattened and asymmetrically broadened, and the $1s3p/1s4p$ -correlated feature around $h\nu = 23.8$ eV is enhanced as compared to the fluorescence spectra for small He droplets ($R \leq 6$ nm). The feature around $h\nu = 24.6$ eV remains sharp in the fluorescence spectra for all sizes, likely due to the contribution of free He atoms and small He clusters accompanying the He droplets in the jet. Note that the fluorescence spectra contain contributions from all singly excited He species decaying to the ground state, whereas ICD spectra are selective to large He droplets which absorb at least two photons in the course of their interaction with the photon beam.

It is also interesting to note that, contrary to the ICD yields shown in Fig. 3(a), the EUV fluorescence yields for large He droplets ($R > 4.5$ nm) are reduced in intensity at the main resonances. This suggests that for large He droplets, where two or more absorption events per droplet become probable, a large fraction of the excited He atoms decay by ICD instead

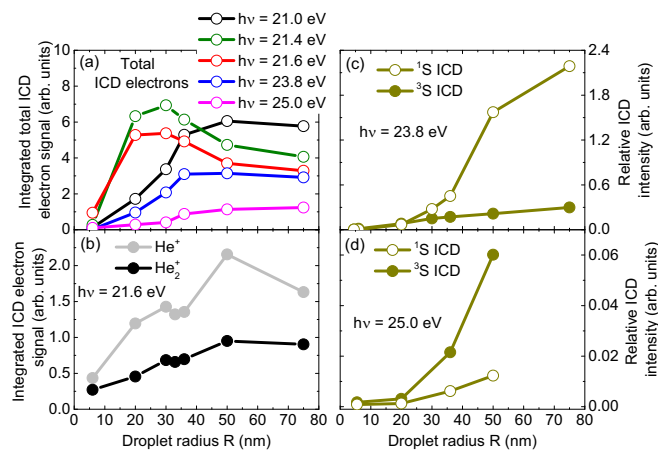


FIG. 4. (a) Droplet-size-dependent total ICD electron yields measured at various photon energies. (b) Integrated ICD signal measured in coincidence with He^+ (gray curve) and He_2^+ (black) at $h\nu = 21.6$ eV and as a function of droplet size. The ICD signals shown in (a) and (b) are normalized to the number of He atoms in the focal volume and the photon flux. [(c) and (d)] Droplet-size-dependent intensity of 1S and 3S ICD electrons relative to photoelectrons measured at $h\nu = 23.8$ eV and at $h\nu = 25.0$ eV, respectively. The estimated uncertainty (statistical and systematic) is 15%, i.e., smaller than the symbol size.

of decaying by fluorescence emission. It would be interesting to quantify the branching ratio of ICD and fluorescence emission. In future experiments both channels should be measured simultaneously.

The most striking feature of the ICD spectra of large He droplets is the enhanced intensity of the peak at $h\nu = 21.0$ eV which becomes the highest peak for droplet sizes $R > 36$ nm. Note that the absorption cross section at the $1s2s\ ^1S$ resonance of medium-sized He droplets is smaller than the absorption cross section of the $1s2p\ ^1P$ resonance by a factor ≈ 7 [47]. The enhancement of the peak at $h\nu = 21.0$ eV for large droplets can also be seen from the total electron spectra shown in Figs. 2(b) and 4(a) which compare droplet-size-dependent ICD electron yields measured at different photon energies. Three regimes can be identified (see Appendix B for a quantitative discussion):

(i) Droplets smaller than a certain size ($R \sim 5$ nm) do not undergo ICD because the average number of excitations per droplet is small, $\langle N_{\text{exc}} \rangle \ll 2$.

(ii) In an intermediate size range ($5 \gtrsim R \gtrsim 50$ nm), the ICD yield rises with increasing droplet size because more and more droplets contain a larger number of He^* 's which all contribute to the ICD signal except one for those droplets where N_{exc} is an odd number.

(iii) In the regime of large droplets ($R \gtrsim 50$ nm) when $N_{\text{exc}} \gg 1$, nearly all He^* 's contribute to ICD and the ICD yield (normalized to the number of He atoms in the interaction volume) saturates. In this regime, the measured ICD rate only depends on the intensity of the radiation, Φ/w^2 .

The change of the structure of the ICD and EUV fluorescence spectra for increasing He droplet sizes $R > 20$ nm may lead to the assumption that the spectra for large He droplets approach the characteristic absorption spectrum of bulk

superfluid He. Intriguingly, the latter (measured in reflection from the surface of liquid He) resembles the spectra measured for small He droplets, though [see the purple line in Fig. 3(b)] [61]. This indicates that the modified peak structure for large He droplets is related to their intrinsic properties. In particular, nano-optical effects, as observed in other types of nanoparticles [62], may be expected to influence the absorption and emission spectra in this range of photon energy and He droplet size.

The limited penetration depth of near-resonant EUV radiation leads to a shadowing effect in He droplets with $R \gtrsim 20$ nm [38]. Accordingly, at the $1s2p\ ^1P$ resonance a larger part of each He droplet is shaded by those He atoms facing toward the incident radiation and the total number of He^* excitations per droplet saturates. This explains the relatively lower ICD yield at the resonance, i.e., in the range $h\nu = 21.3$ – 21.8 eV, than in the ranges next to it, i.e., around $h\nu = 21$ and $h\nu = 22$ eV. The fact that at the weaker $1s2s\ ^1S$ resonance ($h\nu = 21.0$ eV), the ICD yield outgrows that at $h\nu = 21.6$ eV may be due to the smaller amount of energy deposited in the droplet by the He^* relaxation [18,41] which likely raises the probability of the He^* to remain bound to the droplet and decay by ICD.

Additionally, the index of refraction is expected to significantly deviate from 1 by about ± 0.5 in the range ± 0.5 eV around the $1s2p\ ^1P$ droplet resonance peaked at 21.6 eV [63]. In this range, nanofocusing effects may be expected; i.e., the light intensity is concentrated in certain regions of the droplet. This may lead to an enhanced ICD yield because in these regions He^* 's are produced at higher density [16]. Additionally, the wavelength of the EUV radiation, $\lambda = 59$ nm, matches the He droplet size studied here which may lead to resonance effects and the enhancement of the light absorption. Further experiments and simulations should be done to investigate this interesting nano-optical system in detail.

At $h\nu > E_i$, where direct emission of photoelectrons from He droplets is observed [19,46], one would probably not expect to detect any ICD and EUV fluorescence signals. However, both ICD and EUV fluorescence are detected up to $h\nu = 26$ eV or even higher for large He droplets with $R \gtrsim 20$ nm (see the shaded area in Fig. 3). The ICD electron yield appears as a broad feature peaked at $h\nu = E_i = 24.6$ eV which reaches up to $h\nu = 26$ eV. The EUV fluorescence signal appears as a tail that continuously drops even beyond $h\nu = 26$ eV. This indicates that electron-ion recombination is effective for photon energies exceeding E_i by several eV [40,42,49,58,59,64–68]. Electron-ion recombination may be expected to be particularly efficient for $h\nu \lesssim E_i + V_0 = 25.6$ eV, where $V_0 \approx 1$ eV is the gap to the conduction-band edge of superfluid He [57,66,69]. Photoelectrons created with kinetic energy $E_e \lesssim V_0$ promptly localize in the droplet by forming bubbles, which facilitates the recombination with their parent ions. The excited He^* atoms formed in this way subsequently decay either by fluorescence emission or by ICD.

B. Electron-ion coincidence spectra

More detailed insights into the relaxation of large He nanodroplets are obtained from electron and ion spectra recorded

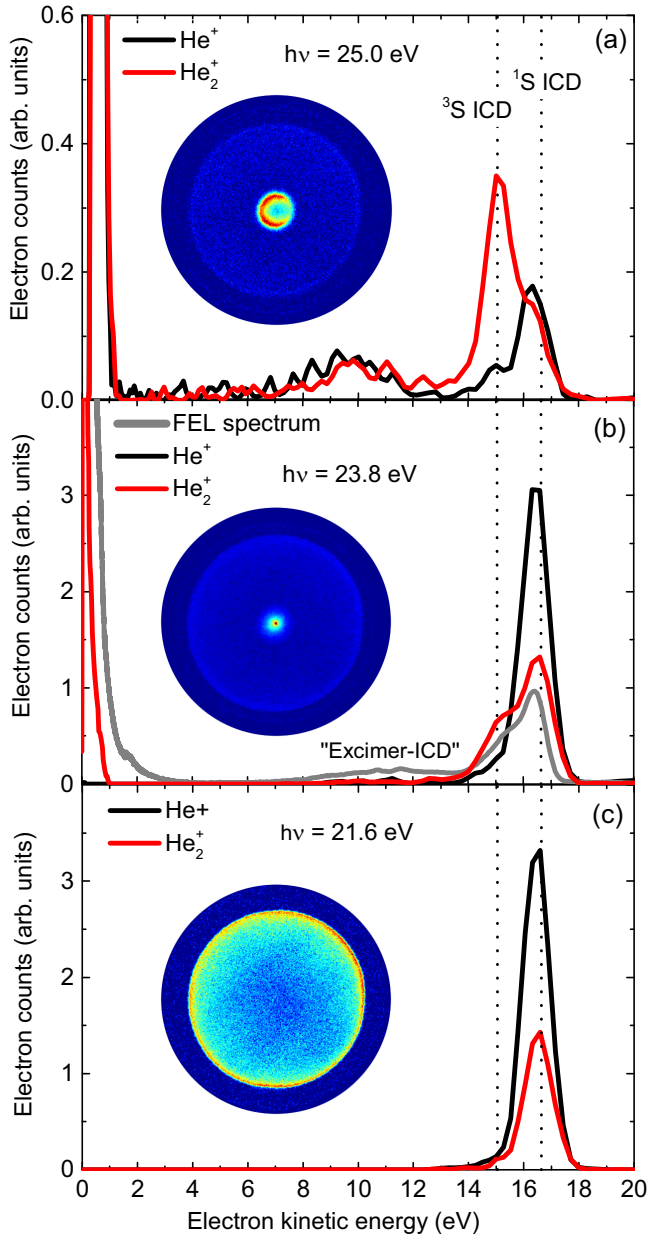


FIG. 5. Background-subtracted electron spectra of large pure He nanodroplet ($R = 50$ nm) measured in coincidence with He^+ and He_2^+ ions at photon energies below and about the ionization energy of He. The two dotted lines indicate the kinetic energies of electrons expected for ICD of two He atoms in their metastable $1s2s\ ^1S$ and $1s2s\ ^3S$ states. Insets show the raw electron VMI in coincidence with He_2^+ . The polarization of the EUV light was vertical (in the paper plane) and the EUV beam was incident on the droplets from the left-hand side. The electron spectra are normalized to the photon flux.

by coincidence detection. Figure 5 shows typical electron spectra measured in coincidence with He^+ (black lines) and He_2^+ (red lines) for large He nanodroplets ($R = 50$ nm) at $h\nu = 25.0$ eV [Fig. 5(a)], 23.8 eV [Fig. 5(b)], and 21.6 eV [Fig. 5(c)]. The corresponding raw electron VMI in coincidence with He_2^+ are displayed as insets. At $h\nu = 21.6$ eV, one sharp-edged, perfectly isotropic ring structure is seen due to ICD electrons. At $h\nu = 23.8$ eV, the ICD ring is still present

but an additional central bright spot appears which is due to emission of electrons by autoionization. At $h\nu = 25$ eV, an anisotropic small ring at the center of the image is due to direct emission of photoelectrons. Note that this ring features a forward-backward asymmetry with respect to the propagation direction of the photon beam due to the shadowing effect [38]. The perfectly isotropic distribution of ICD electrons emitted from large He droplets [see also the inset of Fig. 2(a)] whose photoelectron emission pattern is strongly anisotropic supports the picture of He^* 's emerging to the droplet surface where they redistribute evenly around the droplet prior to ICD.

At $h\nu = 21.6$ eV, both electron spectra measured in coincidence with He^+ and He_2^+ exhibit only one main peak due to ICD of two He^* atoms in the 1S state which is populated by electronic relaxation after exciting the He droplets to the $1s2p\ ^1P$ resonance [45,47].

At $h\nu = 23.8$ eV, the ICD electron spectra measured in coincidence with He_2^+ [Fig. 5(b)] feature a double-peak structure. At this photon energy, the He droplets are excited into the $1s3p$ and $1s4p$ absorption bands [39,40] which then decay by ultrafast electronic relaxation into the $1s2s\ ^1S$ atomic state and by autoionization. The latter pathway can be followed by electron-ion recombination and leads to formation of He_2^* , which in turn either stabilizes in the droplet or dissociates into a ground-state He atom and a He^* preferentially excited in the $1s2s\ ^3S$ state [40,42,58]. Therefore, the shoulder structure at about 15 eV appears at the electron energy expected for two He^* in the 3S state decaying by ICD, $E_e = 2E(^3S) - E_i = 2 \times 19.8\text{ eV} - 24.6\text{ eV} = 15.0\text{ eV}$. The peak at near-zero electron energy is due to electrons emitted by droplet autoionization that do not recombine [19,49].

Note that the 3S ICD feature is only seen in the electron spectrum measured in coincidence with He_2^+ but not in coincidence with He^+ . In contrast, the 1S ICD feature is present in both coincidence electron spectra. This can be seen from the integrated 1S and 3S ICD signals shown in Figs. 13(c) and 13(d) in Appendix D. Thus, 3S ICD generates only He_2^+ ions, whereas 1S ICD generates both He^+ and He_2^+ ions. This points at two different scenarios for ICD in He nanodroplets in the autoionization regime:

(i) He^* atoms excited in the 1S state are formed by electronic relaxation accompanied by the migration of the He^* 's to the droplet surface. There, two He^* 's undergo ICD with only little influence by the He droplet. Accordingly, mostly He^+ ions are produced. Low yields of detected He_2^+ are likely due to the binding of a He atom to the He^+ product as it escapes from the droplet [32,70]. Enhanced formation of He^+ ions compared to He_2^+ by 1S ICD can also be seen from Fig. 4(b) showing integrated 1S ICD signals measured in coincidence with He^+ and He_2^+ at $h\nu = 21.6$ eV as a function of He droplet sizes. Both these 1S ICD signals qualitatively follow the total ICD yields shown in Fig. 4(a).

(ii) He^* atoms in the 3S state are formed by DR of He_2^+ occurring mainly in the bulk of the droplets. Two He^* 's formed in this way undergo ICD prior to their ejection to the droplet surface. Therefore, the resulting He^+ product has a high chance of picking up another He atom to form a He_2^+ which is eventually ejected from the droplet. Associative ionization, i.e., direct formation of stable He_2^+ by ICD, can be ruled out as it is a minor channel [55].

When the photon energy is tuned across E_i up to $h\nu = 25$ eV, direct photoemission becomes the dominant process [see the sharp peak at $E_e = 0.4$ eV in Fig. 5(a) which matches the expected position of the photoline at $E_e = h\nu - E_i$]. Remarkably, ICD features are still clearly visible, implying the presence of two or more neutral excitations in one droplet. In this regime, ICD out of the $1s2s\ ^3S$ state is the main indirect decay channel in the electron spectra measured in coincidence with He_2^+ . Thus, DR which populates the $1s2s\ ^3S$ state appears to contribute more abundantly to the electron- He_2^+ ion coincidences than electronic relaxation which mainly leads to the $1s2s\ ^1S$ state. This can also be seen from the He droplet size dependence of the 1S and 3S ICD components measured at $h\nu = 25.0$ eV [see Fig. 4(d)]. Beyond the onset of ICD at a droplet radius $R \approx 20$ nm, ICD of the 3S state clearly dominates over 1S ICD. The opposite is true at the photon energy $h\nu = 23.8$ eV just above E_i^{drop} [see Fig. 4(c) which is based on the electron spectra shown in Figs. 13(a) and 13(b)].

This enhanced efficiency of 3S ICD over 1S ICD when detecting electron-ion coincidences can be rationalized by the atomic motion occurring in the encounter of two He^* excited atoms along the He_2^{**} potential energy curves (see the pink arrows in Fig. 6 [16]; see Sec. III C for a more detailed discussion). As the potential well depths of the $\text{He}(^3S)\text{-He}(^3S)$ dimer states are twice as deep as for the $\text{He}(^1S)\text{-He}(^1S)$ dimer state, the ion produced by 3S ICD is released with higher kinetic energy and therefore it is ejected out of the He droplet more efficiently. Thus, detection of electron-ion coincidences is more sensitive to 3S ICD which is particularly abundant at higher photon energies $h\nu \gtrsim 25$ eV. This explains our ability to detect ICD up to several eV above E_i using PEPICO-VMI despite a low absolute ICD rate (Fig. 3).

The He_2^+ - and He^+ -correlated electron spectra recorded at $h\nu = 23.8$ eV and $h\nu = 25.0$ eV contain another weak component in the range 7–13 eV that was also seen in FEL experiments at $h\nu = 23.8$ eV [grey line in Fig. 5(b)] [16]. This feature is interpreted as a consequence of ICD involving He_2^* excimers. Interestingly, it is only observed in the electron spectra recorded at $h\nu \geq E_i^{\text{drop}} = 23$ eV and not in the electron spectra at the $1s2p$ resonance at $h\nu = 21.6$ eV [see Fig. 5(c) and Fig. 14 in Appendix D]. This suggests a picture where electron-ion recombination leads to the formation of He_2^* s in He nanodroplets [35,57]. Note that both atomic and molecular triplet emission lines due to relaxation of He_2^* were previously observed in fluorescence spectra of He clusters at $23.1 \leq h\nu \leq 24.6$ eV [42]. Likewise, He_2^* excimers are formed in bulk liquid He following primary ionization [71–74]. While electron recombination with He_2^+ usually is dissociative as mentioned above, inside a He droplet fraction of the He_2^* s formed by recombination can be stabilized by the cold He environment. When the stabilized He_2^* excimer subsequently decays into the electronic ground state by ICD, the amount of energy transferred to the reaction partner (He^* or He_2^*) is significantly lower compared to ICD, where an excited He^* decays to the ground state; the He_2^* excitation energy is lower by 2.5 eV and the He_2 ground-state potential is strongly repulsive at the He_2^* equilibrium distance (1.08 Å) (see the red line in Fig. 6) [75,77]. This He_2^* ICD feature is also observed in large droplets at $h\nu \geq 44.4$ eV where inelastic scattering facilitates the population of excited states [35].

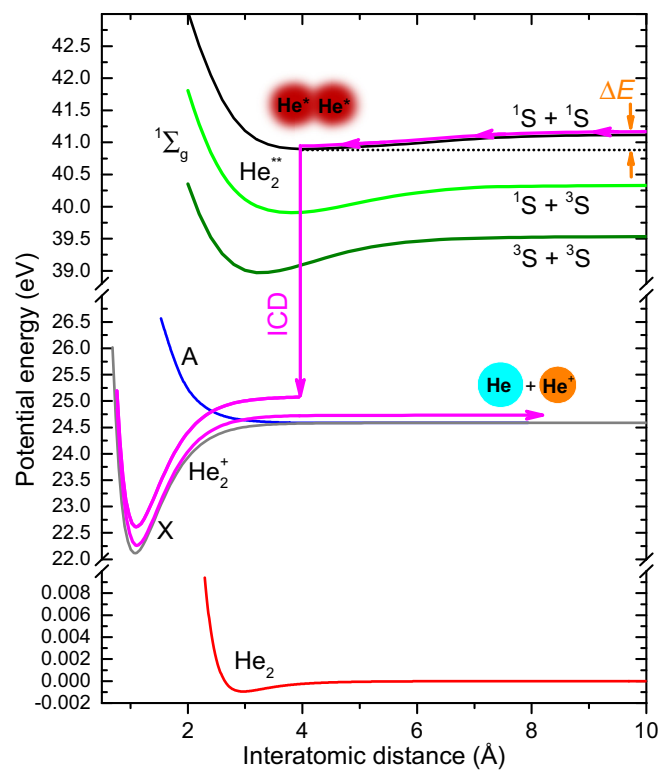


FIG. 6. Potential energy curves of ground-state He_2 (red line) [75], ground and first excited states of He_2^+ (grey and blue lines) [76], and $^1\Sigma_g$ states of doubly excited He_2^{**} (black and green lines) [16]. The pink arrows indicate the atomic motion in the course of ICD of a pair of He^* s along the He_2^{**} and He_2^+ potential energy curves. The two red circles indicate the He_2^{**} excited dimer, while the cyan and orange circles represent the ICD products—a neutral He and a He^+ ion and electron, respectively. The well depth of the He_2^{**} potential ΔE is the maximum potential energy converted into kinetic energy of the two atoms decaying by ICD.

For even higher photon energies we expect that electron-ion recombination becomes the only way of inducing ICD, as the electron promoted into the conduction band detaches from the He^+ core and has to undergo multiple elastic collisions in the droplet to lose enough energy and return to the He^+ . Indeed, when tuning the photon energy from $h\nu = 21.6$ to 28.0 eV, we see a transition from 1S ICD to 3S ICD, and for $h\nu > 25$ eV, 3S ICD clearly dominates the electron spectra measured in coincidence with He_2^+ [see Figs. 7(a) and 7(b)]. Note that the signature of 3S ICD in generating mainly He_2^+ was previously observed for large He nanodroplets irradiated with higher-energy photons at $h\nu > 44.4$ eV where He^* excitation occurs by inelastic collisions of the photoelectron with He atoms in the droplet [35,70]. The ratios of 1S and 3S ICD peak areas versus photoelectrons are shown in Fig. 7(c). They are obtained from fitting Gaussian functions to the 1S and 3S ICD peaks in the electron spectra measured in coincidence with He^+ and He_2^+ , and as the weighted average of their 1S and 3S ICD peak heights, respectively (see Appendix E). Below the He ionization threshold, $h\nu \leq E_i$, the near-zero kinetic energy peak resulting from droplet autoionization is fitted instead of the photoline at $h\nu > E_i$. In this representation of the data, the transition from relaxation-dominated ICD leading

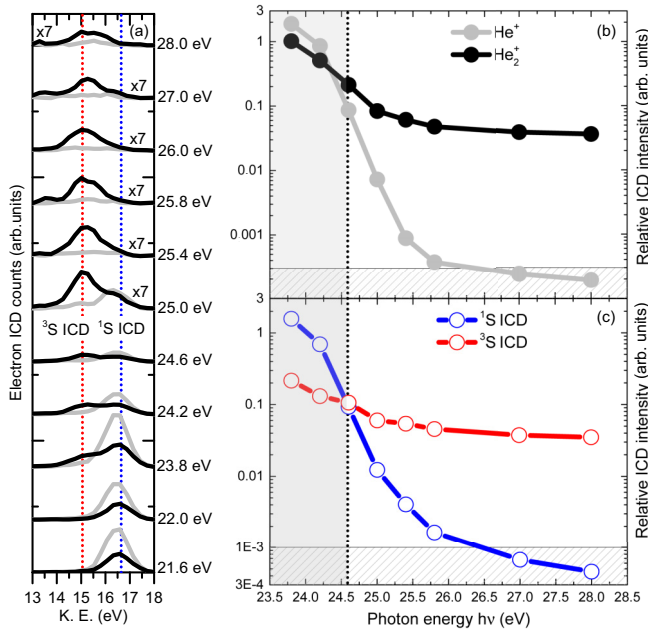


FIG. 7. (a) Background-subtracted ICD electron spectra measured in coincidence with He⁺ (gray lines) and He₂⁺ (black lines) for pure large He nanodroplets ($R = 50$ nm) at different photon energies below and above the He ionization energy E_i . All ICD electron spectra are normalized to the photon flux. All spectra measured at $h\nu \geq 25$ eV are multiplied by a factor of 7 to make the ICD features better visible. The red and blue dotted lines indicate the kinetic energies of an electron emitted by ICD of the ³S and ¹S states, respectively. (b) Yield of ICD electrons relative to photoelectrons recorded in coincidence with He⁺ (gray dots) and He₂⁺ (black dots). (c) Ratio of ¹S (blue dots) and ³S (red dots) ICD electrons to photoelectrons (near-zero-energy electrons for the case $h\nu \leq E_i$). The dashed areas in (b) and (c) indicate the noise floor. The estimated uncertainty (statistical and systematic) is 15%, i.e., smaller than the symbol size.

mostly to ¹S ICD, to recombination-dominated ICD leading to the ³S ICD, occurs right at $h\nu = E_i$. The ¹S ICD signal drops to the noise level for $h\nu \gtrsim 25.5$ eV whereas recombination-induced ICD remains visible even at $h\nu = 28$ eV.

C. Ion kinetic energy distributions

Complementary information about the relaxation dynamics of EUV-irradiated large He droplets is obtained from ion kinetic energy distributions. Figure 8 shows kinetic energy distributions of He⁺ and He₂⁺ ions measured in coincidence with one electron at various photon energies below E_i . The He₂⁺ ion spectra shown in Fig. 8(b) have the same structure with a broad kinetic energy distribution centered around $E_{\text{ion}} = 0.3$ eV that extends up to 1.4 eV.

The majority of He₂⁺ ions detected at $h\nu = 23.8$ and 24.2 eV are created by autoionization (cf. Fig. 5), and their kinetic energy distributions follow the one measured at $h\nu = 25.0$ eV or higher [see Fig. 12(b)], in agreement with previous photoionization measurements [70]. In contrast, ions detected at $h\nu = 21.6$ eV are mainly created by ICD [cf. Fig. 5(c)]. In both cases (autoionization and ICD), the He₂⁺ ions are ejected

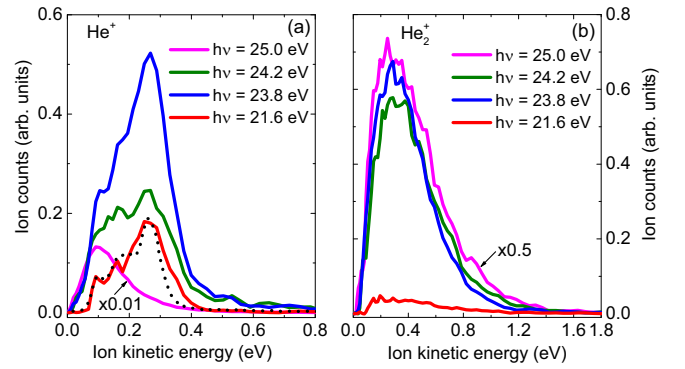


FIG. 8. He⁺ and He₂⁺ ion kinetic energy distributions measured for pure large He nanodroplets of radius $R = 50$ nm at different photon energies below and above the He ionization energy. All ion spectra in (a) and (b) are background subtracted and normalized to the EUV photon flux. The black dotted curve in (a) is obtained by linear transformation of the electron spectrum measured at $h\nu = 21.6$ eV [see red line in Fig. 2(b)] according to Eq. (1).

out of the He droplet by a nonthermal, impulsive process in the course of vibrational relaxation [78].

The kinetic energy distributions of He⁺ ions are shown in Fig. 8(a). Interestingly, all He⁺ ion energy distributions recorded at $h\nu < E_i$ are similar in shape with a pronounced maximum at 0.27 eV. They can only originate from ionization of excited He^{*}s by ICD following two-photon absorption by the droplets. Furthermore, the shape of these spectra clearly differs from the shape of the He⁺ spectrum measured at $h\nu = 25.0$ eV, where only one main broad feature peaking around 0.1 eV with a tail extending to 0.5 eV is observed. The latter broad feature is also visible in the ion spectra recorded for small He droplets. Remarkably, it does not change structure when varying the He droplet size and when tuning the photon energy above E_i [see Fig. 12(a)]. We interpret this generic distribution of ion energies by photoionization into the repulsive A state of the He₂⁺ molecular ion (see the blue line in Fig. 6).

For small He droplets ($R < 20$ nm), an additional sharp peak near 0 eV is present in the ion spectra recorded at $h\nu > E_i$ [see Fig. 12(a)]. It is due to photoionization of the free He atoms accompanying the He droplets in the jet, as discussed in Refs. [38,70]. Note that the He⁺ and He₂⁺ ion spectra recorded at $h\nu > E_i$ for large He nanodroplets ($R > 20$ nm) should include a contribution of He⁺ and He₂⁺ ions created by ICD. However, these ICD ions are hard to identify due to the overwhelming contribution from ions created by direct photoionization.

The proposed relaxation pathway of two He^{*}s formed by absorption of two EUV photons by one He nanodroplet (resonant excitation or electron-ion recombination) leading to the ejection of an ICD electron and ion is illustrated in Fig. 6 [16,75,76]. Following photoexcitation, the two He^{*}s are accelerated toward each other from a large interatomic distance R along the attractive ¹Σ_g potential curve of the doubly excited He dimer, He₂^{**}; when they reach shorter distances R , the ICD probability rises and ICD likely occurs near the well of the potential around $R = 4$ Å, leading to the emission of an ICD electron with an energy corresponding to the difference

potential between the initial He_2^{*} state and the final He_2^+ state at the distance R . The maximum kinetic energy acquired by the two He^* 's is given by the depth of the potential well with respect to the $\text{He}^* + \text{He}^*$ atomic asymptote, ΔE . As the kinetic energy acquired by the two colliding He atoms in the $^1\Sigma_g$ state is not significantly affected by the ICD process, the He and He^+ atoms in the final state continue their trajectory toward short R where they are reflected at the hard-core potential of the He_2^+ ground state X . In this process, the ICD electron energy is reduced to the same extent that the kinetic energy of the products increases in the course of the collision; therefore, the ICD electron spectrum can be transformed into a kinetic energy distribution of the He^+ ICD ion according to

$$E_{\text{ion}} = (2E_{\text{He}^*} - E_i - E_e + dE)/2. \quad (1)$$

Here, $E_{\text{He}^*} = 20.62$ eV is the excitation energy of each He^* atom ($1s2s\ ^1S$ state) and $dE = 0.3$ eV is a droplet-induced energy shift which subsumes the upshift of E_{He^*} [47,70] and the downshift of E_i [19,79] induced by droplet interactions. The factor $1/2$ accounts for equal sharing of the kinetic energy released to the two dissociating He atoms. This calculated ion kinetic energy distribution from the high-resolution electron spectrum measured at $h\nu = 21.6$ eV [red line in Fig. 2(b)] matches the corresponding He^+ ion energy distribution surprisingly well [see the dotted black line in Fig. 8(a)]. This indicates that the He^+ created by ICD is indeed ejected from the He nanodroplet by a binary collisionlike process where the He and He^+ products dissociate without undergoing further scattering. This confirms our conjecture that ICD happens predominantly out of relaxed He^* atoms that have migrated to the He droplet surface.

IV. CONCLUSION

In summary, we have studied in detail the decay of multiply excited He nanodroplets by resonant ICD. Owing to the large absorption cross section of He droplets of sizes $\gtrsim 20$ nm, even low-intensity monochromatic EUV synchrotron radiation can induce multiple excitations in one droplet. Using the advanced techniques of high-resolution electron spectroscopy and PEPICO-VMI, the individual steps of the ICD process out of 1S and 3S states are unraveled at $h\nu$ below and up to a few eV above the helium ionization energy E_i . The main results obtained in this work can be summarized as follows:

(i) At $h\nu = 21.6$ eV where the He nanodroplet is excited into the $1s2p$ -correlated absorption band, the highly resolved electron spectra and the perfectly isotropic distribution of the emitted electrons indicate that ICD takes place between two fully relaxed excited He atoms in metastable states that roam about the He droplet surface. Therefore, this type of ICD may be expected to be a slow process with a time constant on the order of 10 to 100 ps mainly determined by the roaming dynamics.

(ii) The significant changes of the absorption spectrum of large He droplets point at a shadowing effect occurring in such large He nanodroplets resulting in saturation of the number of excited atoms in the droplets at the strongest resonance. Nano-optical effects such as nanofocusing and resonance enhancement of the radiation inside the droplets may play a role as well.

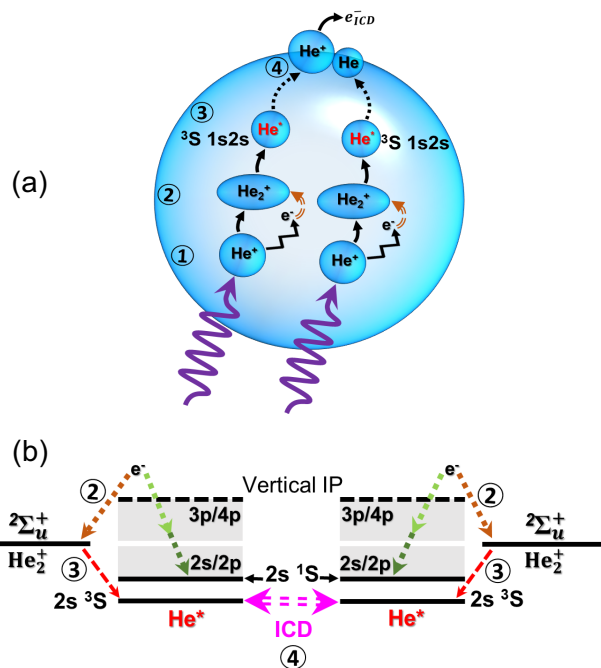


FIG. 9. (a) Schematic illustration of ICD induced by electron-ion recombination in large He droplets following absorption of two ionizing EUV photons. (1) The emitted photoelectrons undergo elastic scattering inside the droplets and lose their kinetic energy. Depending on the excursion time of the electron, the He^+ photoions form stable He_2^+ dimers before recapturing the decelerated electrons (2). Once the electrons have recombined with the ions, excited He_2^* dimers form which dissociate into a ground-state He atom and a He^* in the 3S state (3). The two 3S He^* atoms tend to migrate to the surface of the droplet, where they decay by ICD (4). (b) Energy level diagram illustrating the dynamics (2) by the brown dashed arrow, (3) by the red dashed arrow, and (4) leading to ICD as shown in (a). The green dashed arrows indicate electronic relaxation into the 1S state.

(iii) ICD is efficient even at photon energies exceeding the adiabatic ionization energy of He droplets and up to a few eV above E_i due to electron-ion recombination into excited He states.

(iv) The electron spectra measured in coincidence with He^+ and He_2^+ show that 1S ICD occurs by electronic relaxation in the entire range of resonant photoexcitation, even at $h\nu$ exceeding E_i by about 1 eV.

(v) In the energy range from the adiabatic to the vertical ionization energy of He droplets, a smooth transition occurs from droplet-induced electronic relaxation of excited He to electron-ion recombination by which mainly He^* atoms populated in triplet states are formed.

(vi) In the electron spectra recorded in coincidence with He_2^+ , 3S ICD appears more prominently due to the enhanced ejection of He ions formed in this way; a crossing of the 3S ICD yield and the 1S ICD yield occurs when tuning $h\nu$ across E_i .

(vii) The strongly differing abundances of He^+ and He_2^+ products for 1S vs 3S ICD point at different scenarios of ICD taking place at the surface or in the bulk of the droplets, respectively.

(viii) ICD involving He_2^* excimers occurs only at $h\nu \geq E_i^{\text{drop}}$ due to formation of stabilized He_2^* 's by electron-ion recombination.

The individual steps of the 3S ICD process occurring at $h\nu > E_i$ due to electron-ion recombination are schematically illustrated in Fig. 9. Following photoionization of two He atoms, the emitted electrons perform a diffusionlike motion inside the droplets by which they lose their kinetic energy. Owing to long-range Coulomb attraction, the electrons are drawn back to their parent ions, which tend to form He_2^+ dimer ions by interaction with the surrounding He. Electron-ion recombination then leads to the formation of 3S -excited He^* atoms or $^3\Sigma$ -excited He_2^* excimers. These metastable species are expelled toward the droplet surface, where they meet and decay by ICD.

To assess the general relevance of this process, other types of nanosystems should be studied in a similar size range, e.g., heavier rare-gas clusters and molecular clusters such as water nanodroplets. Some of these can be resonantly excited and ionized with conventional lasers [23]. Electron-ion recombination to create highly reactive excited species may play an even more important role in bulk liquids and biological systems when exposed to ionizing radiation.

ACKNOWLEDGMENTS

M.M. and L.B.L. acknowledge financial support by Deutsche Forschungsgemeinschaft (project BE 6788/1-1), by the Independent Research Fund Denmark (DFR) via Grant No. 1026-00299B, and by the Carlsberg Foundation. We thank the Danish Agency for Science and Higher Education for support through the instrument center DanScatt. S.R.K. thanks the Department of Science and Technology, Government of India, for support through the DST-DAAD scheme and Science and Engineering Research Board. S.R.K. acknowledges support for this research through the Indo-French Center for Promotion of Advanced Research (CEFIPRA). S.R.K., K.S., and S.D. acknowledge the support of the Scheme for Promotion of Academic Research Collaboration, Ministry of Education, Government of India, and the Institute of Excellence programme at IIT-Madras via the Quantum Center for Diamond and Emergent Materials. S.R.K. gratefully acknowledges support of the Max Planck Society's Partner group programme, and M.M. and S.R.K. acknowledge funding from the SPARC Programme, MHRD, India. The research leading to this result has been supported by the project CALIPSOplus under Grant Agreement No. 730872 from the EU Framework Programme for Research and Innovation Horizon 2020 and by the COST Action CA21101 "Confined Molecular Systems: From a New Generation of Materials to the Stars (COSY)."

APPENDIX A: DEPENDENCY OF THE ICD ELECTRON YIELD ON PHOTON FLUX

To probe the dependency of the ICD electron yield on the intensity of the photon beam, we recorded the total yield of ICD electrons with the HEA in the electron energy range $E_e = 16.2\text{--}16.7$ eV at $h\nu = 21.0$ eV and for different droplet sizes R (see Fig. 10). The photon flux was varied by gradually opening and closing the exit slit of the monochromator of the

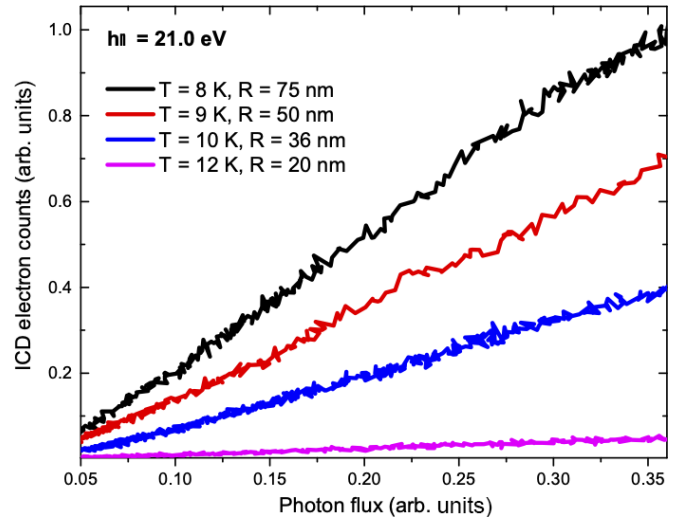


FIG. 10. Yield of ICD electrons as a function of photon flux measured at $h\nu = 21.0$ eV for He droplets of various droplet sizes set by controlling the temperature T of the He nozzle. The photon flux was measured as photocurrents at a photodiode and at a mesh inserted into the photon beam.

beamline. It was measured using a photodiode placed at the end of the beamline as well as by measuring the current at a mesh placed into the photon beam. The latter two currents were perfectly proportional to one another. In the range of lowest photon flux where the slit was nearly fully closed the ICD electron yield appears to show a slightly nonlinear dependency on the photon flux. This may be due to changes in the size and shape of the intensity distribution in the interaction region given by diffraction effects of the light passing through the narrow slit.

APPENDIX B: SIMULATION OF THE He DROPLET SIZE DEPENDENCE OF THE ICD YIELD

In Sec. III A of the main text, the ICD rate is given as $r_{\text{ICD}} = r_{\text{abs}}/2$. This holds for the limit of large droplets when the number of He^* excitations per droplet of mean size $\langle N \rangle$ is large, $\langle N_{\text{exc}} \rangle = p_{\text{He}} \langle N \rangle \gg 1$. Then the number of ICD events is related to the number of excitations per droplet by $N_{\text{ICD}} \approx N_{\text{exc}}/2$. Here, $p_{\text{He}} = \Phi_{\text{tr}} \sigma / w^2 \sim 10^{-7}$ is the excitation probability of a He atom. However, in the regime of small droplets where $N_{\text{exc}} \sim 1$, it becomes relevant that singly excited droplets do not undergo ICD as it takes at least two He^* 's per droplet for ICD to occur. For small numbers $N_{\text{exc}} > 1$, the ICD yield is given by $N_{\text{ICD}} = N_{\text{exc}} // 2$, i.e., by the integer division of N_{exc} by 2. Taking into account that the He droplet sizes follow a normalized linear logarithmic size distribution in the regime of supercritical expansion [80], $P_{\langle N \rangle}(N) = \exp(-N/\langle N \rangle)/\langle N \rangle$, we can model the yield of ICD events as a function of mean droplet size $\langle N \rangle$, normalized to the total density of He atoms, as

$$N_{\text{ICD}}(\langle N \rangle) = \sum_{N_{\text{exc}}=1}^{\infty} P_{\langle N \rangle} \times p_{\text{He}}(N_{\text{exc}}) \frac{N_{\text{exc}} // 2}{N_{\text{exc}}}. \quad (\text{B1})$$

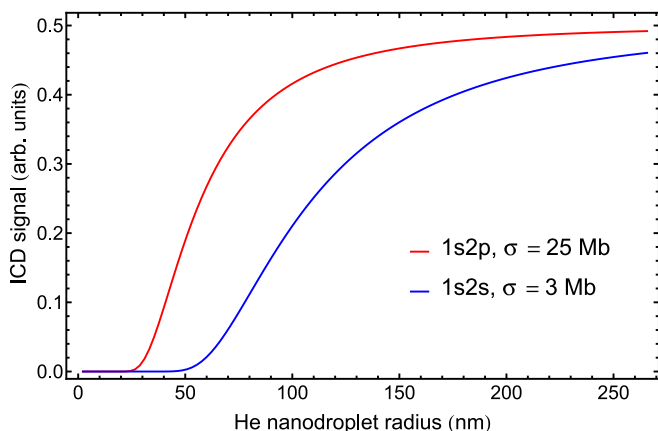


FIG. 11. Simulated yield of ICD events as a function of mean He droplet size for excitation at the $1s2s$ and $1s2p$ resonances.

Here, $P_{(N) \times \rho_{\text{He}}}(N_{\text{exc}})$ is the distribution of the number of He^* excitations for a given mean droplet size. The resulting ICD yield N_{ICD} plotted vs the mean droplet radius $\langle R \rangle = \sqrt[3]{3\langle N \rangle / (4\pi \rho_{\text{He}})}$ is shown in Fig. 11. Here $\rho_{\text{He}} = 22 \text{ nm}^{-3}$ is the number density of He atoms in He nanodroplets.

The resulting model curves show a close resemblance with the experimental data [see Figs. 4(a) and 4(b) in the main text]. The experimental parameters are those given in Secs. II and III of the main text except for the photon flux, which was taken an order of magnitude higher than estimated in Sec. II. Nevertheless, we are confident that the model [Eq. (B1)] captures the essential physics, despite its simplicity.

APPENDIX C: ION KINETIC ENERGY DISTRIBUTIONS

A compilation of He^+ and He_2^+ ion kinetic energy distributions measured for various He nanodroplet radii R and photon energies $h\nu$ is shown in Fig. 12. The He_2^+ spectra have the same shape up to variable amplitude; they all feature a maximum around 0.3 eV and a broad tail that extends up to 1.6 eV. This generic kinetic energy distribution of He_2^+ was previously observed and interpreted by an impulsive ejection

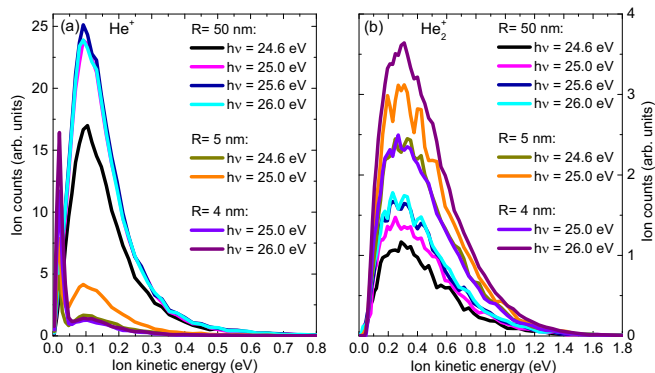


FIG. 12. Ion kinetic energy distributions of (a) He^+ and (b) He_2^+ measured for different droplet conditions and different photon energies $h\nu$ at and above $E_i = 24.6 \text{ eV}$. All the ion spectra in (a) and (b) are background subtracted and normalized to the EUV photon flux.

mechanism [78]. The only remarkable trend is a dropping amplitude for large He droplets ($R = 50 \text{ nm}$). This is likely due to the tendency of large He droplets to efficiently trap ions as any ion tends to solvate in liquid He by forming a dense solvation complex [37].

The He^+ spectra feature two peaks: a sharp one near zero kinetic energy, which is most prominent for small droplets ($R = 4 \text{ nm}$), and a broad one peaked around 0.1 eV, which is present for all values of R and $h\nu$. The former is due to free He atoms accompanying the He droplet jet, whereas the latter is characteristic of photoionization of He nanodroplets. For small nanodroplets the two-photon ionization probability is negligibly small. Therefore, Coulomb explosion of two He^+ photoions created in the same droplet can be ruled out. Moreover, one would expect a shift of the most probable energy of ejected He^+ ions as a function of droplet size as ions created in the bulk of large droplets would likely undergo binary collisions leading to a reduction of their kinetic energy [32]. However, the 0.1-eV feature remains unchanged up to amplitude variations.

Therefore, we rationalize the observation of He^+ ions with kinetic energies peaked at 0.1 eV by photoionization of nearest-neighbor pairs of He atoms into the repulsive A state the He_2^+ molecular ion (see the blue line in Fig. 6 in the main text). The transition from the He_2 ground state to the A state is forbidden in the free He_2 system. However, it may become partly allowed due to symmetry breaking when the transition takes place in the He droplet environment. The estimated ion kinetic energy released following the dissociation along the A -state potential curve is 0.06 eV, which is in decent agreement with the experimental value (0.1 eV).

APPENDIX D: ELECTRON SPECTRA

1. Droplet-size dependence

In addition to Fig. 5 in the main text, further information on the droplet-size-dependent ICD electron yield for pairs

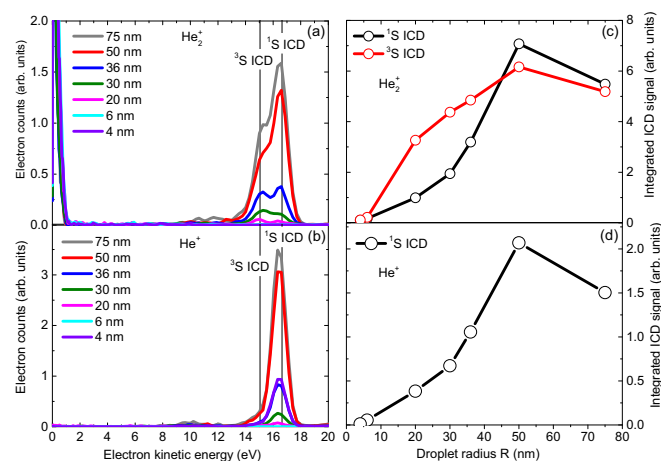


FIG. 13. Electron spectra of He nanodroplets measured in coincidence with (a) He_2^+ and (b) He^+ , respectively, for different He droplet sizes and at $h\nu = 23.8 \text{ eV}$. Integrated (c) 1S and (d) 3S ICD signals measured in coincidence with He_2^+ and He^+ , respectively, and as a function of droplet radius. Both 1S and 3S ICD signals in (c) and (d), respectively, are normalized to the target density.

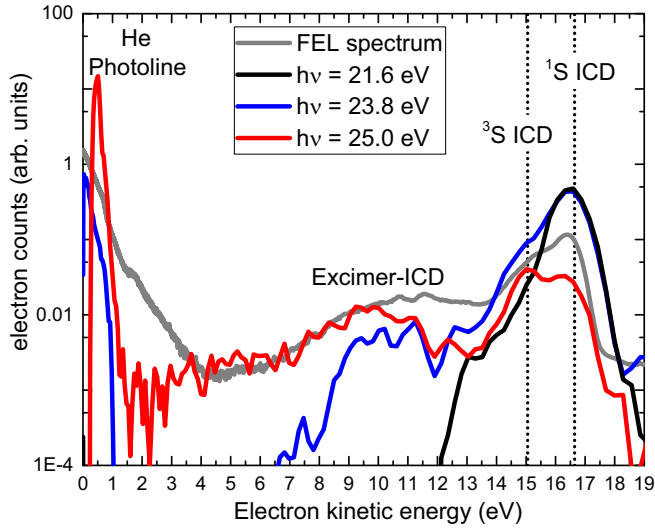


FIG. 14. Logarithmically scaled electron spectra of He nanodroplets measured at different photon energies in comparison with an electron spectrum measured at a FEL at $h\nu = 23.7$ eV. The synchrotron spectra are the sum of the He^+ and He_2^+ electron spectra shown in Figs. 5(a)–5(c) of the main text.

of 1S and 3S He atoms can be obtained from the electron spectra shown in Fig. 13. Figures 13(a) and 13(b) show electron spectra of He nanodroplets of variable droplet sizes ($R = 4.5$ nm up to 75 nm) measured at $h\nu = 23.8$ eV in coincidence with He_2^+ and He^+ , respectively. Clearly, ICD starts to occur for droplets with radius $R \gtrsim 20$ nm and becomes more and more pronounced when the He droplet size increases. Electron spectra measured in coincidence with He^+ exhibit only one feature at 16.6 eV which is assigned to ICD out of the 1S state, whereas the electron spectra measured in coincidence with He_2^+ show two features; one 1S ICD feature at 16.6 eV and one at 15.0 eV attributed to ICD out of the 3S state. The droplet-size dependence of the integrated 1S and 3S ICD electron yields are shown in Figs. 13(c) and 13(d). Surprisingly, the 3S ICD feature in the He_2^+ coincidence spectra appears more pronounced at smaller droplet sizes, whereas at larger droplet sizes $R \gtrsim 40$ nm, the 1S ICD feature again dominates.

2. Photon energy dependence

The coincidence electron spectra measured at $h\nu = 23.8$ eV, presented in Fig. 5(b) in the main text, do not clearly show an excimer ICD feature as the FEL spectrum does. However, in a logarithmic representation of the spectra taken at $h\nu = 21.6, 23.8,$ and 25.0 eV, shown in Fig. 14, an excimer ICD feature is clearly visible.

APPENDIX E: RELATIVE ICD INTENSITY

The relative experimental ICD intensities $I_{\text{ICD}}[\text{He}^+]$ and $I_{\text{ICD}}[\text{He}_2^+]$ plotted in Fig. 7(b) in the main text are obtained from the calculated ratios between the integrated ICD electron yields S measured in coincidence with He^+ and He_2^+ , respectively, and of the photoline. Both of these ratios contain correction factors to account for the second-order radiation ($2h\nu$) present in the photon beam,

$$I_{\text{ICD}}[\text{He}^+] = \frac{S_{\text{ICD}}[\text{He}^+]}{S_{\text{pl}}[\text{He}^+]} - \epsilon_1 \frac{S_{\text{pl}(2h\nu)}[\text{He}^+]}{S_{\text{pl}}[\text{He}^+]}, \quad (\text{E1})$$

$$I_{\text{ICD}}[\text{He}_2^+] = \frac{S_{\text{ICD}}[\text{He}_2^+]}{S_{\text{pl}}[\text{He}_2^+]} - \epsilon_2 \frac{S_{\text{pl}(2h\nu)}[\text{He}_2^+]}{S_{\text{pl}}[\text{He}_2^+]}. \quad (\text{E2})$$

Here, $\epsilon_1 = S_{\text{ICD}(h\nu')}[\text{He}^+]/S_{\text{pl}(h\nu')}[\text{He}^+]$ and $\epsilon_2 = S_{\text{ICD}(h\nu')}[\text{He}_2^+]/S_{\text{pl}(h\nu')}[\text{He}_2^+]$ are taken from Ref. [35] and defined as the efficiency of ICD[He^+] and ICD[He_2^+], respectively, at higher photon energy $h\nu' = 2h\nu \gtrsim 44.4$ eV.

The relative experimental 1S and 3S ICD yields plotted in Fig. 7(c) as well as those plotted in Figs. 4(c) and 4(d) are evaluated by

$$I_{S-\text{ICD}} = \alpha_{1S} \times I_{S\text{ICD}}[\text{He}^+] + \beta_{1S} \times I_{S\text{ICD}}[\text{He}_2^+], \quad (\text{E3})$$

$$I_{S-\text{ICD}} = \alpha_{3S} \times I_{S-\text{ICD}}[\text{He}^+] + \beta_{3S} \times I_{S-\text{ICD}}[\text{He}_2^+]. \quad (\text{E4})$$

Here, $I_{S-\text{ICD}}[\text{He}^+]$ and $I_{S-\text{ICD}}[\text{He}_2^+]$ are obtained separately but in a similar way as in Eq. (1). $I_{S-\text{ICD}}[\text{He}_2^+]$ and $I_{S-\text{ICD}}[\text{He}^+]$ are obtained separately but in a similar way as in Eq. (B1). α_{1S} , β_{1S} , α_{3S} , and β_{3S} are weighting factors:

$$\alpha_{1S} = \frac{A_{1S-\text{ICD}}[\text{He}^+]}{A_{1S-\text{ICD}}[\text{He}^+] + A_{1S-\text{ICD}}[\text{He}_2^+]},$$

$$\beta_{1S} = \frac{A_{1S-\text{ICD}}[\text{He}_2^+]}{A_{1S-\text{ICD}}[\text{He}_2^+] + A_{1S-\text{ICD}}[\text{He}^+]},$$

$$\alpha_{3S} = \frac{A_{3S-\text{ICD}}[\text{He}^+]}{A_{3S-\text{ICD}}[\text{He}^+] + A_{3S-\text{ICD}}[\text{He}_2^+]},$$

$$\beta_{3S} = \frac{A_{3S-\text{ICD}}[\text{He}_2^+]}{A_{3S-\text{ICD}}[\text{He}_2^+] + A_{3S-\text{ICD}}[\text{He}^+]}. \quad (\text{E5})$$

Here $A_{1S-\text{ICD}}[\text{He}^+]$ and $A_{1S-\text{ICD}}[\text{He}_2^+]$ denote the peak heights of the 1S ICD signals measured in coincidence with He^+ and He_2^+ , respectively. $A_{3S-\text{ICD}}[\text{He}^+]$ and $A_{3S-\text{ICD}}[\text{He}_2^+]$ denote the peak heights of the 3S ICD signals measured in coincidence with He^+ and He_2^+ , respectively.

- [1] B. Boudarffa, P. Cloutier, D. Hunting, M. A. Huels, and L. Sanche, Resonant formation of DNA strand breaks by low-energy (3 to 20 eV) electrons, *Science* **287**, 1658 (2000).
 [2] L. S. Cederbaum, J. Zobeley, and F. Tarantelli, Giant intermolecular decay and fragmentation of clusters, *Phys. Rev. Lett.* **79**, 4778 (1997).

- [3] U. Hergenhahn, Interatomic and intermolecular Coulombic decay: The early years, *J. Electron. Spectrosc. Relat. Phenom.* **184**, 78 (2011).
 [4] T. Jahnke, U. Hergenhahn, B. Winter, R. Dörner, U. Fröhling, P. V. Demekhin, K. Gokhberg, L. S. Cederbaum, A. Ehresmann, A. Knie *et al.*, Interatomic

- and intermolecular Coulombic decay, *Chem. Rev.* **120**, 11295 (2020).
- [5] P. Zhang, C. Perry, T. T. Luu, D. Matselyukh, and H. J. Wörner, Intermolecular Coulombic decay in liquid water, *Phys. Rev. Lett.* **128**, 133001 (2022).
- [6] S. Malerz, F. Trinter, U. Hergenbahn, A. Ghrist, H. Ali, C. Nicolas, C.-M. Saak, C. Richter, S. Hartweg, L. Nahon *et al.*, Low-energy constraints on photoelectron spectra measured from liquid water and aqueous solutions, *Phys. Chem. Chem. Phys.* **23**, 8246 (2021).
- [7] S. Barth, S. Joshi, S. Marburger, V. Ulrich, A. Lindblad, G. Öhrwall, O. Björneholm, and U. Hergenbahn, Observation of resonant interatomic Coulombic decay in Ne clusters, *J. Chem. Phys.* **122**, 241102 (2005).
- [8] K. Gokhberg, V. Averbukh, and L. S. Cederbaum, Interatomic decay of inner-valence-excited states in clusters, *J. Chem. Phys.* **124**, 144315 (2006).
- [9] A. I. Kuleff, K. Gokhberg, S. Kopelke, and L. S. Cederbaum, Ultrafast interatomic electronic decay in multiply excited clusters, *Phys. Rev. Lett.* **105**, 043004 (2010).
- [10] E. Allaria, R. Appio, L. Badano, W. Barletta, S. Bassanese, S. Biedron, A. Borgia, E. Busetto, D. Castronovo, P. Cinquegrana *et al.*, Highly coherent and stable pulses from the Fermi seeded free-electron laser in the extreme ultraviolet, *Nat. Photonics* **6**, 699 (2012).
- [11] E. Allaria, A. Battistoni, F. Bencivenga, R. Borghes, C. Callegari, F. Capotondi, D. Castronovo, P. Cinquegrana, D. Cocco, M. Coreno *et al.*, Tunability experiments at the FERMI@Elettra free-electron laser, *New J. Phys.* **14**, 113009 (2012).
- [12] D. Iablonskyi, K. Nagaya, H. Fukuzawa, K. Motomura, Y. Kumagai, S. Mondal, T. Tachibana, T. Takanashi, T. Nishiyama, K. Matsunami, P. Johnsson, P. Piseri, G. Sansone, A. Dubrouil, M. Reduzzi, P. Carpeggiani, C. Vozzi, M. Devetta, M. Negro, F. Calegari, A. Trabattini, M. C. Castrovilli, D. Faccialà, Y. Ovcharenko, T. Möller, M. Mudrich, F. Stienkemeier, M. Coreno, M. Alagia, B. Schütte, N. Berrah, A. I. Kuleff, G. Jabbari, C. Callegari, O. Plekan, P. Finetti, C. Spezzani, E. Ferrari, E. Allaria, G. Penco, C. Serpico, G. De Ninno, I. Nikolov, B. Diviacco, S. Di Mitri, L. Giannessi, K. C. Prince, and K. Ueda, Slow interatomic Coulombic decay of multiply excited neon clusters, *Phys. Rev. Lett.* **117**, 276806 (2016).
- [13] Y. Ovcharenko, V. Lyamayev, R. Katzy, M. Devetta, A. LaForge, P. O’Keeffe, O. Plekan, P. Finetti, M. Di Fraia, M. Mudrich, M. Krikunova, P. Piseri, M. Coreno, N. B. Brauer, T. Mazza, S. Stranges, C. Grazioli, R. Richter, K. C. Prince, M. Drabbels, C. Callegari, F. Stienkemeier, and T. Möller, Novel collective autoionization process observed in electron spectra of He clusters, *Phys. Rev. Lett.* **112**, 073401 (2014).
- [14] A. C. LaForge, M. Drabbels, N. B. Brauer, M. Coreno, M. Devetta, M. Di Fraia, P. Finetti, C. Grazioli, R. Katzy, V. Lyamayev, T. Mazza, M. Mudrich, P. O’Keeffe, Y. Ovcharenko, P. Piseri, O. Plekan, K. C. Prince, R. Richter, S. Stranges, C. Callegari, T. Moller, and F. Stienkemeier, Collective autoionization in multiply-excited systems: A novel ionization process observed in helium nanodroplets, *Sci. Rep.* **4**, 3621 (2014).
- [15] Y. Ovcharenko, A. LaForge, B. Langbehn, O. Plekan, R. Cucini, P. Finetti, P. O’Keeffe, D. Iablonskyi, T. Nishiyama, K. Ueda *et al.*, Autoionization dynamics of helium nanodroplets resonantly excited by intense XUV laser pulses, *New J. Phys.* **22**, 083043 (2020).
- [16] A. C. LaForge, R. Michiels, Y. Ovcharenko, A. Ngai, J. M. Escartín, N. Berrah, C. Callegari, A. Clark, M. Coreno, R. Cucini, M. Di Fraia, M. Drabbels, E. Fasshauer, P. Finetti, L. Giannessi, C. Grazioli, D. Iablonskyi, B. Langbehn, T. Nishiyama, V. Oliver, P. Piseri, O. Plekan, K. C. Prince, D. Rupp, S. Stranges, K. Ueda, N. Sisourat, J. Eloranta, M. Pi, M. Barranco, F. Stienkemeier, T. Möller, and M. Mudrich, Ultrafast resonant interatomic Coulombic decay induced by quantum fluid dynamics, *Phys. Rev. X* **11**, 021011 (2021).
- [17] J. P. Toennies, A. F. Vilesov, and K. B. Whaley, Superfluid helium droplets: An ultracold nanolaboratory, *Phys. Today* **54**, 31 (2001).
- [18] M. Mudrich, A. LaForge, A. Ciavardini, P. O’Keeffe, C. Callegari, M. Coreno, A. Demidovich, M. Devetta, M. Di Fraia, M. Drabbels *et al.*, Ultrafast relaxation of photoexcited superfluid He nanodroplets, *Nat. Commun.* **11**, 112 (2020).
- [19] D. S. Peterka, J. H. Kim, C. C. Wang, L. Poisson, and D. M. Neumark, Photoionization dynamics of pure helium droplets, *J. Phys. Chem. A* **111**, 7449 (2007).
- [20] M. Kelbg, M. Zabel, B. Krebs, L. Kazak, K.-H. Meiwes-Broer, and J. Tiggesbäumker, Auger emission from the Coulomb explosion of helium nanoplasmas, *J. Chem. Phys.* **150**, 204302 (2019).
- [21] L. Ben Ltaief, M. Shcherbinin, S. Mandal, S. Krishnan, A. LaForge, R. Richter, S. Turchini, N. Zema, T. Pfeifer, E. Fasshauer *et al.*, Charge exchange dominates long-range interatomic Coulombic decay of excited metal-doped helium nanodroplets, *J. Phys. Chem. Lett.* **10**, 6904 (2019).
- [22] M. Kirm, S. Vielhauer, G. Zimmerer, V. Kisand, E. Sombrowski, and B. Steeg, Prompt and delayed secondary excitons in rare gas solids, *J. Low Temp. Phys.* **29**, 822 (2003).
- [23] P. Y. Serdobintsev, A. S. Melnikov, A. A. Pastor, N. A. Timofeev, and M. A. Khodorkovskiy, Relaxation times measurement in single and multiply excited xenon clusters, *J. Chem. Phys.* **148**, 194301 (2018).
- [24] B. Schütte, M. Arbeiter, T. Fennel, G. Jabbari, A. Kuleff, M. Vrakking, and A. Rouzée, Observation of correlated electronic decay in expanding clusters triggered by intense near-infrared fields, *Nat. Commun.* **6**, 8596 (2015).
- [25] T. Oelze, B. Schütte, M. Müller, J. P. Müller, M. Wieland, U. Frühling, M. Drescher, A. Al-Shemmary, T. Golz, N. Stojanovic *et al.*, Correlated electronic decay in expanding clusters triggered by intense XUV pulses from a free-electron-laser, *Sci. Rep.* **7**, 40736 (2017).
- [26] M. Kelbg, M. Zabel, B. Krebs, L. Kazak, K.-H. Meiwes-Broer, and J. Tiggesbäumker, Temporal development of a laser-induced helium nanoplasma measured through Auger emission and above-threshold ionization, *Phys. Rev. Lett.* **125**, 093202 (2020).
- [27] G. Soavi, S. Dal Conte, C. Manzoni, D. Viola, A. Narita, Y. Hu, X. Feng, U. Hohenester, E. Molinari, D. Prezzi *et al.*, Exciton-exciton annihilation and biexciton stimulated emission in graphene nanoribbons, *Nat. Commun.* **7**, 11010 (2016).
- [28] A. Lewis, A. Ruseckas, O. Gaudin, G. Webster, P. Burn, and I. Samuel, Singlet exciton diffusion in MEH-PPV films studied by exciton-exciton annihilation, *Org. Electron.* **7**, 452 (2006).

- [29] N. Kumar, Q. Cui, F. Ceballos, D. He, Y. Wang, and H. Zhao, Exciton-exciton annihilation in MoSe₂ monolayers, *Phys. Rev. B* **89**, 125427 (2014).
- [30] G. Delport, G. Chehade, F. Lédée, H. Diab, C. Milesi-Brault, G. Trippe-Allard, J. Even, J.-S. Lauret, E. Deleporte, and D. Garrot, Exciton-exciton annihilation in two-dimensional halide perovskites at room temperature, *J. Phys. Chem. Lett.* **10**, 5153 (2019).
- [31] A. C. LaForge, V. Stumpf, K. Gokhberg, J. von Vangerow, F. Stienkemeier, N. V. Kryzhevoi, P. O’Keeffe, A. Ciavardini, S. R. Krishnan, M. Coreno, K. C. Prince, R. Richter, R. Moshhammer, T. Pfeifer, L. S. Cederbaum, and M. Mudrich, Enhanced ionization of embedded clusters by electron-transfer-mediated decay in helium nanodroplets, *Phys. Rev. Lett.* **116**, 203001 (2016).
- [32] M. Shcherbinin, A. C. LaForge, V. Sharma, M. Devetta, R. Richter, R. Moshhammer, T. Pfeifer, and M. Mudrich, Interatomic Coulombic decay in helium nanodroplets, *Phys. Rev. A* **96**, 013407 (2017).
- [33] F. Wiegandt, F. Trinter, K. Henrichs, D. Metz, M. Pitzer, M. Waitz, E. Jabbour al Maalouf, C. Janke, J. Rist, N. Wechselberger, T. Miteva, S. Kazandjian, M. Schöffler, N. Sisourat, T. Jahnke, and R. Dörner, Direct observation of interatomic Coulombic decay and subsequent ion-atom scattering in helium nanodroplets, *Phys. Rev. A* **100**, 022707 (2019).
- [34] L. B. Ltaief, M. Shcherbinin, S. Mandal, S. Krishnan, R. Richter, T. Pfeifer, M. Bauer, A. Ghosh, M. Mudrich, K. Gokhberg *et al.*, Electron transfer mediated decay of alkali dimers attached to He nanodroplets, *Phys. Chem. Chem. Phys.* **22**, 8557 (2020).
- [35] L. Ben Ltaief, K. Sishodia, S. Mandal, S. De, S. R. Krishnan, C. Medina, N. Pal, R. Richter, T. Fennel, and M. Mudrich, Efficient indirect interatomic Coulombic decay induced by photoelectron impact excitation in large pure helium nanodroplets, *Phys. Rev. Lett.* **131**, 023001 (2023).
- [36] R. Michiels, M. Abu-samaha, L. B. Madsen, M. Binz, U. Bangert, L. Bruder, R. Duim, A. Wituschek, A. C. LaForge, R. J. Squibb, R. Feifel, C. Callegari, M. Di Fraia, M. Danailov, M. Manfredda, O. Plekan, K. C. Prince, P. Rebernik, M. Zangrando, F. Stienkemeier, and M. Mudrich, Enhancement of above threshold ionization in resonantly excited helium nanodroplets, *Phys. Rev. Lett.* **127**, 093201 (2021).
- [37] J. D. Asmussen, L. Ben Ltaief, K. Sishodia, A. R. Abid, B. Bastian, S. Krishnan, H. B. Pedersen, and M. Mudrich, Dopant ionization and efficiency of ion and electron ejection from helium nanodroplets, *J. Chem. Phys.* **159**, 034301 (2023).
- [38] J. D. Asmussen, K. Sishodia, B. Bastian, A. R. Abid, L. B. Ltaief, H. B. Pedersen, S. De, C. Medina, N. Pal, R. Richter, T. Fennel, S. Krishnan, and M. Mudrich, Electron energy loss and angular asymmetry induced by elastic scattering in superfluid helium nanodroplets, *Nanoscale* **15**, 14025 (2023).
- [39] M. P. Ziemkiewicz, D. M. Neumark, and O. Gessner, Ultrafast electronic dynamics in helium nanodroplets, *Int. Rev. Phys. Chem.* **34**, 239 (2015).
- [40] J. D. Asmussen, R. Michiels, K. Dulitz, A. Ngai, U. Bangert, M. Barranco, M. Binz, L. Bruder, M. Danailov, M. Di Fraia, J. Eloranta, R. Feifel, L. Giannessi, M. Pi, O. Plekan, K. C. Prince, R. J. Squibb, D. Uhl, A. Wituschek, M. Zangrando, C. Callegari, F. Stienkemeier, and M. Mudrich, Unravelling the full relaxation dynamics of superexcited helium nanodroplets, *Phys. Chem. Chem. Phys.* **23**, 15138 (2021).
- [41] A. LaForge, J. Asmussen, B. Bastian, M. Bonanomi, C. Callegari, S. De, M. Di Fraia, L. Gorman, S. Hartweg, S. Krishnan *et al.*, Relaxation dynamics in excited helium nanodroplets probed with high resolution, time-resolved photoelectron spectroscopy, *Phys. Chem. Chem. Phys.* **24**, 28844 (2022).
- [42] K. von Haefen, A. R. B. de Castro, M. Joppien, L. Moussavizadeh, R. von Pietrowski, and T. Möller, Discrete visible luminescence of helium atoms and molecules desorbing from helium clusters: The role of electronic, vibrational, and rotational energy transfer, *Phys. Rev. Lett.* **78**, 4371 (1997).
- [43] P. O’Keeffe, P. Bolognesi, M. Coreno, A. Moise, R. Richter, G. Cautero, L. Stebel, R. Sergo, L. Pravica, Y. Ovcharenko, and L. Avaldi, A photoelectron velocity map imaging spectrometer for experiments combining synchrotron and laser radiations, *Rev. Sci. Instrum.* **82**, 033109 (2011).
- [44] B. Dick, Inverting ion images without Abel inversion: Maximum entropy reconstruction of velocity maps, *Phys. Chem. Chem. Phys.* **16**, 570 (2014).
- [45] D. Buchta, S. R. Krishnan, N. B. Brauer, M. Drabbels, P. O’Keeffe, M. Devetta, M. Di Fraia, C. Callegari, R. Richter, M. Coreno, K. C. Prince, F. Stienkemeier, R. Moshhammer, and M. Mudrich, Charge transfer and Penning ionization of dopants in or on helium nanodroplets exposed to EUV radiation, *J. Phys. Chem. A* **117**, 4394 (2013).
- [46] D. Buchta, S. R. Krishnan, N. B. Brauer, M. Drabbels, P. O’Keeffe, M. Devetta, M. Di Fraia, C. Callegari, R. Richter, M. Coreno, K. C. Prince, F. Stienkemeier, J. Ullrich, R. Moshhammer, and M. Mudrich, Extreme ultraviolet ionization of pure He nanodroplets: Mass-correlated photoelectron imaging, Penning ionization, and electron energy-loss spectra, *J. Chem. Phys.* **139**, 084301 (2013).
- [47] M. Joppien, R. Karnbach, and T. Möller, Electronic excitations in liquid helium: The evolution from small clusters to large droplets, *Phys. Rev. Lett.* **71**, 2654 (1993).
- [48] R. Fröchtenicht, U. Henne, J. P. Toennies, A. Ding, M. Fieber-Erdmann, and T. Drewello, The photoionization of large pure and doped helium droplets, *J. Chem. Phys.* **104**, 2548 (1996).
- [49] D. S. Peterka, A. Lindinger, L. Poisson, M. Ahmed, and D. M. Neumark, Photoelectron imaging of helium droplets, *Phys. Rev. Lett.* **91**, 043401 (2003).
- [50] C. C. Wang, O. Kornilov, O. Gessner, J. H. Kim, D. S. Peterka, and D. M. Neumark, Photoelectron imaging of helium droplets doped with Xe and Kr atoms, *J. Phys. Chem.* **112**, 9356 (2008).
- [51] M. Shcherbinin, A. C. LaForge, M. Hanif, R. Richter, and M. Mudrich, Penning ionization of acene molecules by helium nanodroplets, *J. Phys. Chem. A* **122**, 1855 (2018).
- [52] A. LaForge, M. Shcherbinin, F. Stienkemeier, R. Richter, R. Moshhammer, T. Pfeifer, and M. Mudrich, Highly efficient double ionization of mixed alkali dimers by intermolecular Coulombic decay, *Nat. Phys.* **15**, 247 (2019).
- [53] S. Mandal, R. Gopal, M. Shcherbinin, A. D’Elia, H. Srinivas, R. Richter, M. Coreno, B. Bapat, M. Mudrich, S. Krishnan, and V. Sharma, Penning spectroscopy and structure of acetylene oligomers in He nanodroplets, *Phys. Chem. Chem. Phys.* **22**, 10149 (2020).
- [54] J. P. Toennies and A. F. Vilesov, Superfluid helium droplets: A uniquely cold nanomatrix for molecules and molecular complexes, *Angew. Chem.* **43**, 2622 (2004).

- [55] M. W. Müller, W. Bussert, M. W. Ruf, H. Hotop, and W. Meyer, New oscillatory structure in electron energy spectra from autoionizing quasi-molecules: Subthermal collisions of He(2^3S) atoms with He($2^1S, 2^3S$) atoms, *Phys. Rev. Lett.* **59**, 2279 (1987).
- [56] M. Müller, A. Merz, M.-W. Ruf, H. Hotop, W. Meyer, and M. Movre, Experimental and theoretical studies of the bi-excited collision systems He*(2^3S) + He*($2^3S, 2^1S$) at thermal and subthermal kinetic energies, *Z. Phys. D* **21**, 89 (1991).
- [57] H. Buchenau, J. P. Toennies, and J. A. Northby, Excitation and ionization of ^4He clusters by electrons, *J. Chem. Phys.* **95**, 8134 (1991).
- [58] H. B. Pedersen, H. Buhr, S. Altevogt, V. Andrianarijaona, H. Kreckel, L. Lammich, N. de Ruelle, E. M. Staicu-Casagrande, D. Schwalm, D. Strasser, X. Urbain, D. Zajfman, and A. Wolf, Dissociative recombination and low-energy inelastic electron collisions of the helium dimer ion, *Phys. Rev. A* **72**, 012712 (2005).
- [59] L. Carata, A. E. Orel, and A. Suzor-Weiner, Dissociative recombination of He_2^+ molecular ions, *Phys. Rev. A* **59**, 2804 (1999).
- [60] K. von Haefen, T. Laarmann, H. Wabnitz, T. Möller, and K. Fink, Size and isotope effects of helium clusters and droplets: Identification of surface and bulk-volume excitations, *J. Phys. Chem. A* **115**, 7316 (2011).
- [61] C. M. Surko, G. J. Dick, F. Reif, and W. C. Walker, Spectroscopic study of liquid helium in the vacuum ultraviolet, *Phys. Rev. Lett.* **23**, 842 (1969).
- [62] R. Signorell, M. Goldmann, B. L. Yoder, A. Bodi, E. Chasovskikh, L. Lang, and D. Luckhaus, Nanofocusing, shadowing, and electron mean free path in the photoemission from aerosol droplets, *Chem. Phys. Lett.* **658**, 1 (2016).
- [63] D. Rupp, N. Monserud, B. Langbehn, M. Sauppe, J. Zimmermann, Y. Ovcharenko, T. Möller, F. Frassetto, L. Poletto, A. Trabattini *et al.*, Coherent diffractive imaging of single helium nanodroplets with a high harmonic generation source, *Nat. Commun.* **8**, 493 (2017).
- [64] L. Coman, M. Guna, L. Simons, and K. A. Hardy, First measurement of the rotational constants for the homonuclear molecular ion He_2^+ , *Phys. Rev. Lett.* **83**, 2715 (1999).
- [65] X. Urbain, N. Djurić, C. Safvan, M. Jensen, H. Pedersen, L. V. Søgaard, and L. Andersen, Storage ring study of the dissociative recombination of He_2^+ , *J. Phys. B* **38**, 43 (2005).
- [66] K. von Haefen, T. Laarmann, H. Wabnitz, and T. Möller, The electronically excited states of helium clusters: An unusual example for the presence of Rydberg states in condensed matter, *J. Phys. B* **38**, S373 (2005).
- [67] J. Royal and A. E. Orel, Resonant dissociative excitation and vibrational excitation of He_2^+ , *Phys. Rev. A* **75**, 052706 (2007).
- [68] H. Buhr, H. B. Pedersen, S. Altevogt, V. M. Andrianarijaona, H. Kreckel, L. Lammich, S. Novotny, D. Strasser, J. Hoffmann, M. Lange, M. Lestinsky, M. B. Mendes, M. Motsch, O. Novotný, D. Schwalm, X. Urbain, D. Zajfman, and A. Wolf, Inelastic electron collisions of the isotopically symmetric helium dimer ion $^4\text{He}_2^+$ in a storage ring, *Phys. Rev. A* **77**, 032719 (2008).
- [69] A. Mauracher, O. Echt, A. Ellis, S. Yang, D. Bohme, J. Postler, A. Kaiser, S. Denifl, and P. Scheier, Cold physics and chemistry: Collisions, ionization and reactions inside helium nanodroplets close to zero K, *Phys. Rep.* **751**, 1 (2018).
- [70] M. Shcherbinin, F. Westergaard, M. Hanif, S. Krishnan, A. LaForge, R. Richter, T. Pfeifer, and M. Mudrich, Inelastic scattering of photoelectrons from He nanodroplets, *J. Chem. Phys.* **150**, 044304 (2019).
- [71] A. Benderskii, R. Zadoyan, N. Schwentner, and V. Apkarian, Photodynamics in superfluid helium: Femtosecond laser-induced ionization, charge recombination, and preparation of molecular Rydberg states, *J. Chem. Phys.* **110**, 1542 (1999).
- [72] J. Gao, A. Marakov, W. Guo, B. Pawlowski, S. Van Sciver, G. Ihas, D. McKinsey, and W. Vinen, Producing and imaging a thin line of He_2^* molecular tracers in helium-4, *Rev. Sci. Instrum.* **86**, 093904 (2015).
- [73] W. Dennis, E. Durbin, Jr., W. Fitzsimmons, O. Heybey, and G. Walters, Spectroscopic identification of excited atomic and molecular states in electron-bombarded liquid helium, *Phys. Rev. Lett.* **23**, 1083 (1969).
- [74] J. Hill, O. Heybey, and G. Walters, Evidence of metastable atomic and molecular bubble states in electron-bombarded superfluid liquid helium, *Phys. Rev. Lett.* **26**, 1213 (1971).
- [75] X. Sheng, J. P. Toennies, and K. T. Tang, Conformal analytical potential for all the rare gas dimers over the full range of internuclear distances, *Phys. Rev. Lett.* **125**, 253402 (2020).
- [76] A. Carrington, C. H. Pyne, and P. J. Knowles, Microwave electronic spectrum of the He_2^+ ion, *J. Chem. Phys.* **102**, 5979 (1995).
- [77] S. L. Fiedler and J. Eloranta, Interaction of helium Rydberg state atoms with superfluid helium, *J. Low Temp. Phys.* **174**, 269 (2014).
- [78] B. E. Callicoatt, K. Förde, L. F. Jung, T. Ruchti, and K. C. Janda, Fragmentation of ionized liquid helium droplets: A new interpretation, *J. Chem. Phys.* **109**, 10195 (1998).
- [79] M. Theisen, F. Lackner, G. Krois, and W. E. Ernst, Ionization thresholds of alkali metal atoms on helium droplets, *J. Phys. Chem. Lett.* **2**, 2778 (2011).
- [80] E. L. Knuth and U. Henne, Average size and size distribution of large droplets produced in a free-jet expansion of a liquid, *J. Chem. Phys.* **110**, 2664 (1999).